The Astrophysical Journal Letters, 994:L45 (25pp), 2025 December 1 https://doi.org/10.3847/2041-8213/ae17a8

Optimizing Kilonova Searches: A Case Study of the Type IIb SN 2025ulz in the Localization Volume of the Low-significance Gravitational Wave Event S250818k

Noah Franz[1], Bhagya Subrayan[1], Charles D. Kilpatrick[2], Griffin Hosseinzadeh[3], David J. Sand[1], Kate D. Alexander[1], Wen-fai Fong[2,4], Collin T. Christy[1], Jeniveve Pearson[1], Tanmoy Laskar[5], Brian Hsu[1], Jillian Rastinejad[6,29], Michael J. Lundquist[7], Edo Berger[8], K. Azalee Bostroem[1], Clecio R. Bom[9], Phelipe Darc[9], Mark Gurwell[8], Shelbi Hostler Schimpf[8], Garrett K. Keating[8], Phillip Noel[1], Conor Ransome[1], Ramprasad Rao[8], Luidhy Santana-Silva[9], A. Souza Santos[9], Manisha Shrestha[10], Ramya Anche[1], Jennifer E. Andrews[11], Sanchayeeta Borthakur[12], Nathaniel R. Butler[12], Deanne L. Coppejans[13], Philip N Daly[1], Kathryne J. Daniel[1], Paul C. Duffell[14], Tarraneh Eftekhari[2], Carl E. Fields[1], Alexander T. Gagliano[8,15,16], Walter W. Golay[8], Aldana Grichener[1], Erika T. Hamden[1], Daichi Hiramatsu[17], Harsh Kumar[8,15], Vikram Manikantan[1], Raffaella Margutti[18,19,20], Vasileios Paschalidis[1,21], Kerry Paterson[22], Daniel E. Reichart[23], Mathieu Renzo[1], Kali Salmas[24], Genevieve Schroeder[25], Nathan Smith[1], Kristine Spekkens[26], Jay Strader[27], David E. Trilling[28], Nicholas Vieira[2], Benjamin Weiner[24], and Peter K. G. Williams[8]

[1] Department of Astronomy and Steward Observatory, University of Arizona, 933 North Cherry Avenue, Tucson, AZ 85721-0065, USA; nfranz@arizona.edu
[2] Center for Interdisciplinary Exploration and Research in Astrophysics and Department of Physics and Astronomy, Northwestern University, 1800 Sherman Avenue, 8th Floor, Evanston, IL 60201, USA
[3] Department of Astronomy Astrophysics, University of California, San Diego, 9500 Gilman Drive, MC 0424, La Jolla, CA 92093-0424, USA
[4] Department of Physics and Astronomy, Northwestern University, Evanston, IL 60208, USA
[5] Department of Physics Astronomy, University of Utah, Salt Lake City, UT 84112, USA
[6] Department of Astronomy, University of Maryland, College Park, MD 20742-2421, USA
[7] W. M. Keck Observatory, 65-1120 Māmalahoa Highway, Kamuela, HI 96y43-8431, USA
[8] Center for Astrophysics | Harvard & Smithsonian, 60 Garden Street, Cambridge, MA 02138-1516, USA
[9] Laboratório de Inteligência Artificial, Centro Brasileiro de Pesquisas Físicas, 138 Rua Doutor Xavier Sigaud 150, CEP 22290-180, 139 Rio de Janeiro, RJ, Brazil
[10] School of Physics and Astronomy, Monash University, Clayton, Victoria 3800, Australia
[11] Gemini Observatory/NSF's NOIRLab, 670 North A'ohoku Place, Hilo, HI 96720, USA
[12] School of Earth and Space Exploration, Arizona State University, P.O. Box 871404, Tempe, AZ 85287-1404, USA
[13] Department of Physics, University of Warwick, Coventry CV 4 7AL, UK
[14] Department of Physics and Astronomy, Purdue University, 525 Northwestern Avenue, West Lafayette, IN 47907, USA
[15] The NSF AI Institute for Artificial Intelligence and Fundamental Interactions,77 Massachusetts Avenue, 26-555 Cambridge, MA 02139, USA
[16] Department of Physics and Kavli Institute for Astrophysics and Space Research, Massachusetts Institute of Technology, 77 Massachusetts Avenue, Cambridge, MA 02139, USA
[17] Department of Astronomy, University of Florida, 211 Bryant Space Science Center, Gainesville, FL 32611-2055, USA
[18] Department of Astronomy, University of California, Berkeley, CA 94720-3411, USA
[19] Berkeley Center for Multi-messenger Research on Astrophysical Transients and Outreach (Multi-RAPTOR), University of California,12 Berkeley, CA 94720-3411, USA
[20] Department of Physics, University of California, 366 Physics North MC 7300, Berkeley, CA 94720, USA
[21] Department of Physics, University of Arizona, Tucson, AZ 85721, USA
[22] Max-Planck-Institut für Astronomie, Königstuhl 17, 69117 Heidelberg, Germany
[23] Department of Physics and Astronomy, University of North Carolina at Chapel Hill, Campus Box 3255, Chapel Hill, NC 27599-3255, USA
[24] MMT and Steward Observatory, University of Arizona, 933 North Cherry Avenue, Tucson, AZ 85721-0065, USA
[25] Department of Astronomy, Cornell University, Ithaca, NY 14853, USA
[26] Department of Physics, Engineering Physics and Astronomy, Queen's University, Kingston, ON, K7L 2E1, Canada
[27] Center for Data Intensive and Time Domain Astronomy, Department of Physics and Astronomy, Michigan State University, East Lansing, MI 48824, USA
[28] Department of Astronomy and Planetary Science, Northern Arizona University, PO Box 6010, Flagstaff, AZ 86011, USA
Received 2025 October 19; revised 2025 October 23; accepted 2025 October 24; published 2025 November 25

Abstract

Kilonovae, the ultraviolet/optical/infrared counterparts to binary neutron star mergers, are an exceptionally rare class of transients. Optical follow-up campaigns are plagued by contaminating transients, which may mimic kilonovae but do not receive sufficient observations to measure the full photometric evolution. In this work, we present an analysis of the multiwavelength dataset of supernova (SN) 2025ulz, a proposed kilonova candidate following the low-significance detection of gravitational waves originating from the potential binary neutron star merger S250818k. Despite an early rapid decline in brightness, our multiwavelength observations of SN 2025ulz reveal that it is a type IIb SN. As part of this analysis, we demonstrate the capabilities of a novel quantitative scoring algorithm to determine the likelihood that a transient candidate is a kilonova, based primarily on its three-dimensional location and light-curve evolution. We also apply our scoring algorithm to other transient candidates

[29] NHFP Einstein Fellow.

in the localization volume of S250818k and find that, at all times after the discovery of SN 2025ulz, there are $\geqslant$4 candidates with a score comparable to SN 2025ulz, indicating that the kilonova search may have benefited from the additional follow-up of other candidates. During future kilonova searches, this type of scoring algorithm will be useful to rule out contaminating transients in real time, optimizing the use of valuable telescope resources.

Unified Astronomy Thesaurus concepts: Core-collapse supernovae (304); Supernovae (1668); Gravitational wave astronomy (675); Gravitational waves (678); Gravitational wave sources (677); Time domain astronomy (2109)

Materials only available in the online version of record: machine-readable tables

1. Introduction

The detection of gravitational waves (GWs) associated with the binary neutron star (BNS) merger GW170817 by the LIGO Scientific Collaboration & Virgo Collaboration (2017), and the subsequent discovery of GW170817's electromagnetic counterparts (LIGO Scientific Collaboration et al. 2017a), GRB 170817A (I. Arcavi et al. 2017a; A. Goldstein et al. 2017; V. Savchenko et al. 2017) and AT 2017gfo (D. A. Coulter et al. 2017; V. M. Lipunov et al. 2017; S. J. Smartt et al. 2017; M. Soares-Santos et al. 2017; N. R. Tanvir et al. 2017; S. Valenti et al. 2017), opened a powerful new window on our Universe. The unambiguous association of the short gamma-ray burst (SGRB) GRB 170817A and kilonova (KN) AT 2017gfo (LIGO Scientific Collaboration et al. 2017a) provided unique insights into the relativistic engine driving SGRBs (K. D. Alexander et al. 2017; W. Fong et al. 2017; LIGO Scientific Collaboration et al. 2017b; R. Margutti et al. 2017; A. Murguia-Berthier et al. 2021; V. Savchenko et al. 2017), the properties of neutron stars (NSs; e.g., their equation of state; LIGO Scientific Collaboration & Virgo Collaboration 2018; D. Radice et al. 2018), and the formation of *r*-process elements in the ejecta of BNS mergers (I. Arcavi et al. 2017b; P. S. Cowperthwaite et al. 2017; M. R. Drout et al. 2017; M. M. Kasliwal et al. 2017; C. D. Kilpatrick et al. 2017; S. J. Smartt et al. 2017; N. R. Tanvir et al. 2017).

Theoretical models (e.g., D. Kasen et al. 2015, 2017; B. D. Metzger 2017; B. D. Metzger et al. 2024; Y.-X. Chen & B. D. Metzger 2025), combined with observations of AT 2017gfo, demonstrate that photometric observations can typically discriminate between KNe and other transient types. After a BNS merger occurs, *r*-process nucleosynthesis in the neutron-rich ejecta forms heavy *r*-process elements, including lanthanides and actinides (B. D. Metzger et al. 2010). The radioactive decay of the heavy elements heats the ejecta, resulting in a faint and rapidly fading (few days to a week) transient whose spectral energy distribution (SED) primarily peaks in the near-infrared (L.-X. Li & B. Paczynski 1998; J. Barnes & D. Kasen 2013; M. Tanaka & K. Hotokezaka 2013; B. D. Metzger 2017). If the merger remnant launches outflows, it may (primarily depending on the neutron mass in the ejecta) inject energy and result in a rebrightening of the light curve in the infrared, while only resulting in a "plateau" in the optical (D. Kasen et al. 2015).

Beyond GW170817, searches for an electromagnetic counterpart associated with a GW signal have been unsuccessful (I. Andreoni et al. 2019, 2020; M. W. Coughlin et al. 2019; D. Dobie et al. 2019, 2021; D. A. Goldstein et al. 2019; S. Gomez et al. 2019; G. Hosseinzadeh et al. 2019; M. J. Lundquist et al. 2019; K. Ackley et al. 2020; S. Antier et al. 2020a, 2020b; A. Garcia et al. 2020; B. P. Gompertz et al. 2020; M. M. Kasliwal et al. 2020; R. Morgan et al. 2020; A. S. Pozanenko et al. 2020; A. L. Thakur et al. 2020; N. Vieira et al. 2020; A. M. Watson et al. 2020; K. D. Alexander et al. 2021; S. Anand et al. 2021; R. L. Becerra et al. 2021; D. Bhakta et al. 2021; S.-W. Chang et al. 2021; S. de Wet et al. 2021; S. Dichiara et al. 2021; C. D. Kilpatrick et al. 2021; O. R. McBrien et al. 2021; S. R. Oates et al. 2021; T. Ohgami et al. 2021; K. Paterson et al. 2021; T. de Jaeger et al. 2022; J. C. Rastinejad et al. 2022; D. L. Tucker et al. 2022; T. Ahumada et al. 2024, 2025; P. Darc et al. 2025; D. Frostig et al. 2025; J. H. Gillanders et al. 2025; L. Hu et al. 2025; G. S. H. Paek et al. 2025; M. Pillas et al. 2025). During these searches, there are often many transients that are spatially and temporally colocated with a given GW event, a subset of which are new, extragalactic events. Some of these contaminants are impostors, which have light curves that are initially faint and rapidly declining, appearing similar to a KN for several days, but eventually evolving away from expectations (O. R. McBrien et al. 2021; T. Barna et al. 2025). Quickly ruling out interloping transients in real time will help the community focus their follow-up efforts on more promising candidates.

Due to their initial rapid decline, type IIb supernovae (SNe IIb) are common KN impostors (T. Barna et al. 2025). SNe IIb are characterized by weak hydrogen absorption lines at early times ($\sim$weeks to months after explosion) and likely originate from a progenitor star with a partially stripped hydrogen envelope (P. Podsiadlowski et al. 1993; M. W. Richmond et al. 1994; S. E. Woosley et al. 1994; T. Matheson et al. 2000; A. Elmhamdi et al. 2006; R. A. Chevalier & A. M. Soderberg 2010). Importantly, SNe IIb can feature a double-peaked light curve in the ultraviolet, optical, and infrared (e.g., K. Matthews et al. 2002). The first peak ($\sim$few days after explosion) is dominated by shock breakout and subsequent cooling (M. W. Richmond et al. 1994; I. Arcavi et al. 2017a; K. K. Das et al. 2023). The initial shock cooling lasts $\sim$ 5–7 days, after which the radioactive decay of ^{56}Ni heats the ejecta and dominates the observed emission, powering the second peak (e.g., P. J. Benson et al. 1994). In addition to their initial rapid decline, this rebrightening may appear similar to the "plateau" phase of a KN light curve. But, conventional KN models are unable to reproduce a significant rebrightening in the optical for more than a few days (D. Kasen et al. 2015, 2017).

In this Letter, we focus on electromagnetic candidates potentially associated with the subthreshold GW event S250818k, a GW event with a 29% probability of being a BNS merger and a 71% probability of being of terrestrial origin (LIGO Scientific Collaboration et al. 2025a; LIGO Scientific Collaboration et al. 2025b). In particular, we present our observations of SN 2025ulz,[30] including new observational evidence that SN 2025ulz is a type IIb SN and not a KN counterpart to S250818k. We find that both the photometric

[30] We consistently refer to the transient as "SN 2025ulz," rather than "AT 2025ulz," since this is the official IAU name on the Transient Name Server.

evolution and spectrum are consistent with other SNe IIb and inconsistent with both AT 2017gfo and a suite of KNe models.

We also present a novel algorithm for quantifying the likelihood that a specific electromagnetic counterpart is associated with a BNS or neutron star–black hole (NSBH) GW event. We apply this algorithm to SN 2025ulz and the 120 other transients discovered (1) within one week of the putative merger and (2) within the 95% localization region of S250818k. We find ∼1–2 candidates have a photometric evolution roughly consistent with a KN. But, these ∼2 candidates only have two to five publicly available photometry points, making it unclear if any of them are true KNe. Through this analysis, we demonstrate the current capabilities of this quantitative scoring algorithm. In the future, we will continue development of this algorithm and make it available as part of a publicly available web application.

This Letter is organized as follows. Section 2 describes the discovery and initial public observations of S250818k and SN 2025ulz. Section 3 provides the details of our follow-up observations, spanning ultraviolet to radio wavelengths. In Section 4, we analyze our observations and discuss the implications for the interpretation of SN 2025ulz as an SN IIb. In Section 5, we describe our search for additional KN candidates associated with S250818k. Finally, we summarize and conclude in Section 6. Throughout this work, we assume a flat ΛCDM cosmology with $H_0 = 69.6\,\mathrm{km\,s^{-1}\,Mpc^{-1}}$ (W. L. Freedman et al. 2020).

2. Discovery of S250818k and SN 2025ulz

The GW event S250818k was initially discovered by the LIGO/Virgo/KAGRA (LVK) Collaboration as a subthreshold event detected at 2025 August 18 01:20:19 UTC (GPS time: 1439515224.03) and reported at 2025 August 18 01:20:35 UTC. Preliminary classification of the event from the `pycbc` pipeline yielded a 29% probability of being a BNS merger and a 71% probability of being a Terrestrial event (LIGO Scientific et al. 2025a). This initial classification also yielded a 50th (90th) percentile confidence sky localization that spanned 205 deg^2 (786 deg^2) with a posterior luminosity distance of 259 ± 62 Mpc. S250818k has a false alarm rate, also estimated by the `pycbc` online analysis pipeline (S. A. Usman et al. 2016), of 6.81×10^{-8} Hz (1 per 170 days), close to the reported LVK threshold for significant events after accounting for the trials factor[31] (e.g., see S. S. Chaudhary et al. 2024, for a full description of these parameters). We note that the probability that the system had an NS (`HasNS`) and the probability that the system ejected a nonzero amount of NS matter (`HasRemnant`) were both estimated to be 1.0, under the assumption that the event was nonterrestrial.

The revised S250818k event analysis (i.e., the "initial" analysis), provided on 2025 August 20 04:52:51 UTC (∼48 hr after the first alert), and the S250818k "update" analysis, provided on 2025 August 20 09:57:08 UTC, changed these parameters slightly (see, e.g., LIGO Scientific Collaboration et al. 2025a; LIGO Scientific Collaboration et al. 2025b). Given the short gap between these updates, we provide only the latter here, which we use for the majority of our analysis. The final event classification changed only marginally and remained consistent with a 29% probability of being a BNS merger and 71% probability of being Terrestrial. Similarly, the false alarm rate remained at 6.81×10^{-8} Hz. The final `Bilby` offline analysis map expanded the localization slightly to a 50th (90th) percentile sky localization of 276 deg^2 (949 deg^2) with a corresponding all-sky distance constraint of 237 ± 62 Mpc (Figure 1). Finally, we note that the `Bilby` analysis revised the `HasNS` and `HasRemnant` estimates down to 0.8 each, while the chirp mass estimate placed >99% of the probability within the (0.1, 0.87) $M_\odot$ bin.

On 2025 August 18 17:01:30 UTC, ∼16 hr after the initial GW alert, R. Stein et al. (2025) reported the discovery of a potential electromagnetic counterpart to S250818k: SN 2025ulz. Following this, at ∼2.6 days after the discovery of S250818k, V. Karambelkar et al. (2025) reported that the most likely host galaxy of SN 2025ulz has a spectroscopic redshift $z = 0.0848$ (D ≈ 360 Mpc). This distance is somewhat consistent with the distance to S250818k along the line of sight to SN 2025ulz, with a ≈68% joint probability of the transient and GW distance distributions (see subsections 5.2 and 5.6). This motivated a global follow-up campaign with facilities covering the X-ray through radio wavelengths (e.g., J. H. Gillanders et al. 2025, in the optical). Subsequent messages posted on the General Coordinates Network (GCN) over the next ∼3 days reported photometry consistent with a fast-fading red transient with a similar decay rate to AT 2017gfo (X. J. Hall et al. 2025), but ∼1.5 orders of magnitude more luminous. The source was never detected in the X-ray (R. L. Becerra et al. 2025a; X. J. Hall et al. 2025; R. Z. Li et al. 2025; M. Nakajima et al. 2025). A source was detected in the radio by the MeerKAT telescope (G. Bruni et al. 2025b, 2025c) but this emission was diffuse and later shown to likely be associated with the host galaxy (G. Bruni et al. 2025d; L. Rhodes et al. 2025). The source was not detected with any other radio telescope (G. Bruni et al. 2025a; R. Ricci et al. 2025b, 2025d). The basic properties of SN 2025ulz are summarized in Table 1.

On 2025 August 23 15:18:41 UTC, ∼5 days after the discovery of S250818k, J. Freeburn et al. (2025) reported a rebrightening in the *i*-band light curve of SN 2025ulz, and subsequent GCNs confirmed this finding (C. Angulo et al. 2025; R. L. Becerra et al. 2025c; J. H. Gillanders et al. 2025), making the light curve more consistent with a SN IIb rather than AT 2017gfo or other plausible KN emission. Soon after, a new spectrum confirmed the presence of a broad ($v \sim 15{,}600\,\mathrm{km\,s^{-1}}$) P-Cygni H$\alpha$ line, consistent with other SN IIb at this phase (S. Banerjee et al. 2025). Despite this, SN 2025ulz continued to be observed and the exact origin remains hotly debated (e.g., J. H. Gillanders et al. 2025; M. M. Kasliwal et al. 2025). J. H. Gillanders et al. (2025) searched the S250818k localization region with Pan-STARRS and found no promising candidate KNe, concluding that SN 2025ulz is qualitatively consistent with a SN classification and incompatible with KN models.

3. Multiwavelength Follow-up Observations of SN 2025ulz

Given the strong temporal and spatial association of SN 2025ulz with S250818k, we observed it from the ultraviolet to radio wavelengths. In the following subsections we describe these previously unreported observations. All optical photometry and spectra will be made public on WISeREP (O. Yaron & A. Gal-Yam 2012), and the radio observations and optical photometry will be made public,

[31] See description in https://emfollow.docs.ligo.org/userguide/analysis/index.html#alert-threshold-trial-factor.

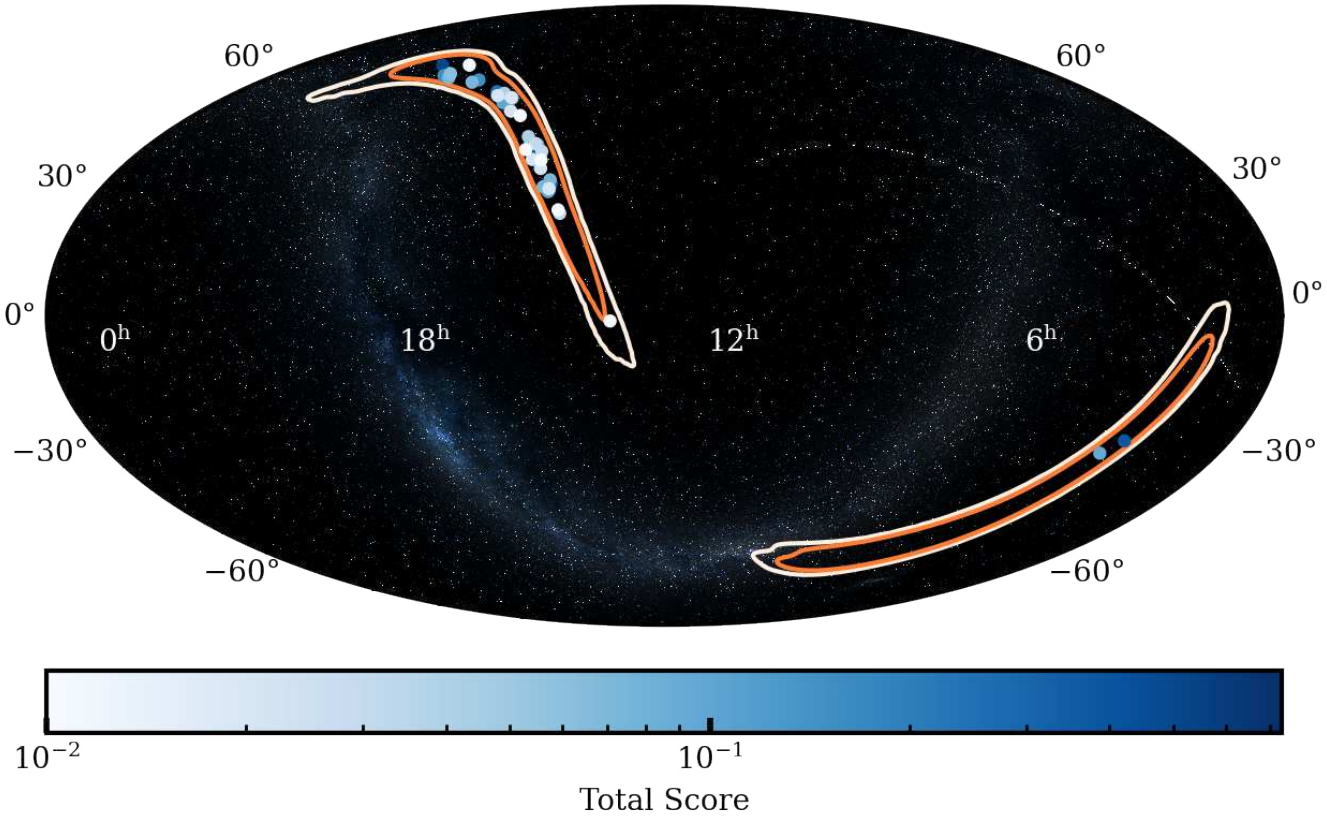

Figure 1. The International Gravitational Wave Network skymap credibility contours (orange: 50%, white: 90%) of S250818k, and the locations of all 121 candidates we found within the 95% credibility region from the Transient Name Server. The color of the point represents the overall score from our vetting, which is described in Section 5.

jointly, on the Open mulTiwavelength Transient Event Repository (OTTER; N. Franz et al. 2025). All photometry is also provided in Appendix C.

3.1. Public Photometry

We gather the publicly available data reported on the GCN and the TNS for SN 2025ulz. This includes the ultraviolet, optical, infrared, and radio observations reported in GCN circulars (with the exception of the MeerKAT data, which we reanalyze ourselves; Section 3.4). We also include the photometry from J. H. Gillanders et al. (2025).

Using the methodology described in G. Hosseinzadeh et al. (2024), we also query the Asteroid Terrestrial-impact Last Alert System (ATLAS; J. L. Tonry et al. 2018) forced photometry server (K. W. Smith et al. 2020; L. Shingles et al. 2021) at the coordinates of SN 2025ulz from ∼180 days prior to ∼20 days after it was discovered. ATLAS forced photometry subtractions are based on difference images and are subject to false detections attributed to bad subtractions, potentially due to artifacts in template images. Therefore, for SN 2025ulz, we consider an ATLAS forced photometry observation to be a detection if it (1) is significant at the 5σ level and (2) has at least two other 5σ detections within a 10 day window.

3.2. Optical Photometry

The site of SN 2025ulz was observed over multiple epochs with the Hubble Space Telescope (HST) using the Wide Field Camera 3 (WFC3) as part of GO-17450 and GO-17805 (PI: Troja). The counterpart and its host galaxy were imaged in the F336W, F606W, F110W, and F160W bands from 22 to 28 August 2025. We downloaded all HST images of SN 2025ulz from the Mikulski Archive for Space Telescopes[32] and processed them with `hst123` (see C. D. Kilpatrick 2021; C. D. Kilpatrick et al. 2021), including frame-to-frame alignment with `Tweakreg` and image coaddition with `astrodrizzle` (STSCI Development Team. 2012), and photometry in the calibrated image frames with `dolphot` (A. Dolphin 2016). We obtain detections of SN 2025ulz in every epoch and band, and we provide the corresponding photometry in Table 4 (Appendix C). A false color image of a subset of the HST imaging from 26 to 28 August 2025 in the F606W, F110W, and F160W bands is given in Figure 2.

We observed SN 2025ulz in *ri* bands on 2025 August 22 and *iz* bands on 2025 August 30 using the imaging mode of the Binospec instrument (D. Fabricant et al. 2019) on the 6.5 m MMT telescope located on Mt. Hopkins in Arizona, USA. We processed all imaging using the `POTPyRI` pipeline[33] (see, e.g., Y. Dong et al. 2024; CHIME/FRB Collaboration et al. 2025). We calibrate photometric zero-points using stars in the Panoramic Survey Telescope and Rapid Response System (Pan-STARRS; K. C. Chambers et al. 2016) data release (DR) 1 photometric survey. We derive an effective point-spread function (ePSF) model for each processed image by fitting

[32] doi:10.17909/echw-bs67
[33] https://github.com/CIERA-Transients/POTPyRI

Table 1
SN 2025ulz Properties

Property	Value	Source
R.A.	$15^{h}51^{m}54^{s}.201$	R. Stein (2025)
Decl.	$+30^{d}54^{m}08^{s}.67$	R. Stein (2025)
Redshift	0.0848	V. Karambelkar et al. (2025)
$E(B-V)_{MW}$	0.0243 mag	D. J. Schlegel et al. (1998); E. F. Schlafly & D. P. Finkbeiner (2011)
Host SFR	$\sim 1\ M_{\odot}\ \ \mathrm{yr}^{-1}$	D. O. Jones et al. (2024); this work (Section 4.4)
Envelope Mass (RSG)	$0.027^{+0.009}_{-0.007}\ M_{\odot}$	This work (Section 4.2)
Progenitor Radius (RSG)	$0.6^{+1.6}_{-0.4} \times 10^{13}$ cm	This work (Section 4.2)
Envelope Mass (BSG)	$0.14^{+0.08}_{-0.04}\ M_{\odot}$	This work (Section 4.2)
Progenitor Radius (BSG)	$0.5^{+2.0}_{-0.3} \times 10^{13}$ cm	This work (Section 4.2)

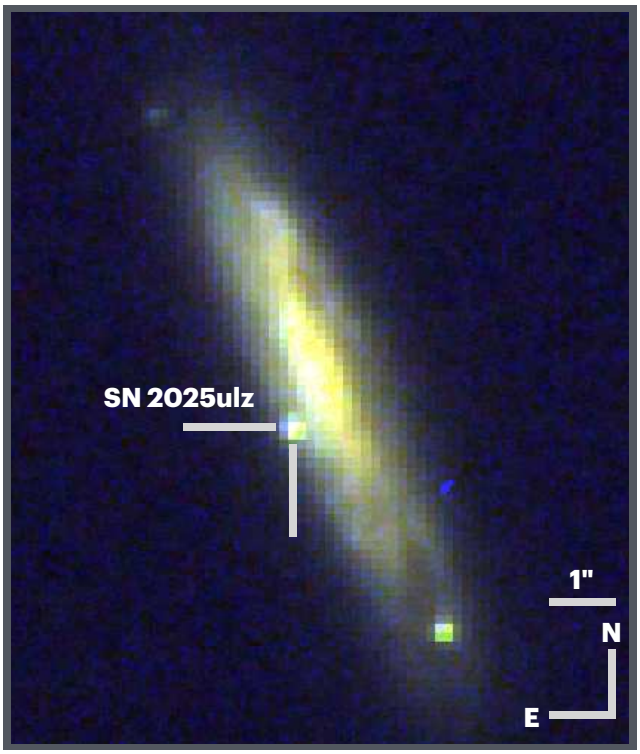

Figure 2. A false color image of the HST WFC3 observations of SN 2025ulz. We include the F606W image from August 26 (blue; $\delta t \sim 8$ days), the F110W image from August 27 (green; $\delta t \sim 9$ days), and the F160W image from 2025 August 28 (red; $\delta t \sim 10$ days). We highlight the position of SN 2025ulz showing its close in projection to the core of its host galaxy.

bright, isolated stars with the `EPSFBuilder` tool from the `photutils` package in `Astropy`. We then perform point-spread function (PSF)-fitting at the location of SN 2025ulz, as well as a set of 20 or more stars spread throughout the image. A first-order two-dimensional polynomial is included in the PSF fitting to account for any spatially varying background and to avoid overfitting of the stars. To estimate the uncertainty of each flux measurement, we set the statistical uncertainty per pixel using the rms error of the fit residuals scaled by a factor of the square root of the reduced χ^2. We then multiply this value by the number of 'noise pixels' of the ePSF.[34] We use the set of Pan-STARRS calibration stars to derive aperture corrections ($\lesssim$0.1 mag in all filters) to scale PSF-fitting magnitudes to the images' photometric zero-points. For the total uncertainty in our reported magnitudes, we report the statistical flux uncertainty summed in quadrature with the rms error of the stars used in the zero-point and ePSF aperture correction. Despite the large field of view of Binospec, the limited number of isolated stars in the Pan-STARRS catalog results in the zero-point rms dominating the reported error. For photometry taken on 2025 August 22, we report 5σ limits. The limiting magnitude is calculated by placing 50 random background apertures within 70 pixels from the target position and taking the standard deviation of the aperture values. We then repeat this 10 times and choose σ to be the average of the 10 runs. Finally, we convert the 5σ flux in counts to magnitude using the photometric zero-point derived from the calibration stars.

We observed SN 2025ulz on 2025 August 28 with the Goodman High-throughput Spectrograph (J. C. Clemens et al. 2004) in imaging mode on the Southern Astrophysical Research Telescope (SOAR) on Cerro Pachon, Chile. We used *riz* bands with a single 100 s frame and 3×200 s images in each band. All SOAR/Goodman imaging data were processed using `photpipe` (A. Rest et al. 2005) using methods described in J. C. Rastinejad et al. (2025). We calibrated all data using bias and dome flat-field frames obtained on the same night and instrumental configuration and aligned to the Gaia DR3 astrometric frame (Gaia Collaboration et al. 2023) using point-like astrometric standards. We then performed PSF photometry in each frame using a custom version of `dophot` (P. L. Schechter et al. 1993) and calibrated the photometry using Pan-STARRS DR2 *riz* photometric standards in each image (H. A. Flewelling et al. 2020). We then resampled each image to a common, undistorted astrometric frame and stacked images in each band with `Swarp` (E. Bertin 2010). SN 2025ulz is located close to the nucleus of its host galaxy, and so we subtracted Pan-STARRS 3π images in each band using `hotpants` (A. Becker 2015). We detect a faint residual in *i* band in the subtracted images and we place 3σ upper limits on the presence of a counterpart in *r* and *z* bands using forced aperture photometry within 2.5× the full width at half-maximum of the difference image PSF and at the location of SN 2025ulz.

We observed SN 2025ulz over multiple epochs starting on 2025 August 21 with the T80N-Cam on the Observatorio Astrofísico de Javalambre (OAJ) 83 cm telescope located at the Astrophysical Observatory in Teruel, Spain. We observed in *r* and *i* bands with 2×300 s in *r* band and 4×300 s in *i* band. All imaging was processed following the same procedures as with the SOAR imaging, including Pan-STARRS subtractions, using the S-PLUS Transient Extension

[34] A derivation of this quantity by F. Masci can be found at http://web.ipac.caltech.edu/staff/fmasci/home/mystats/noisepix_specs.pdf

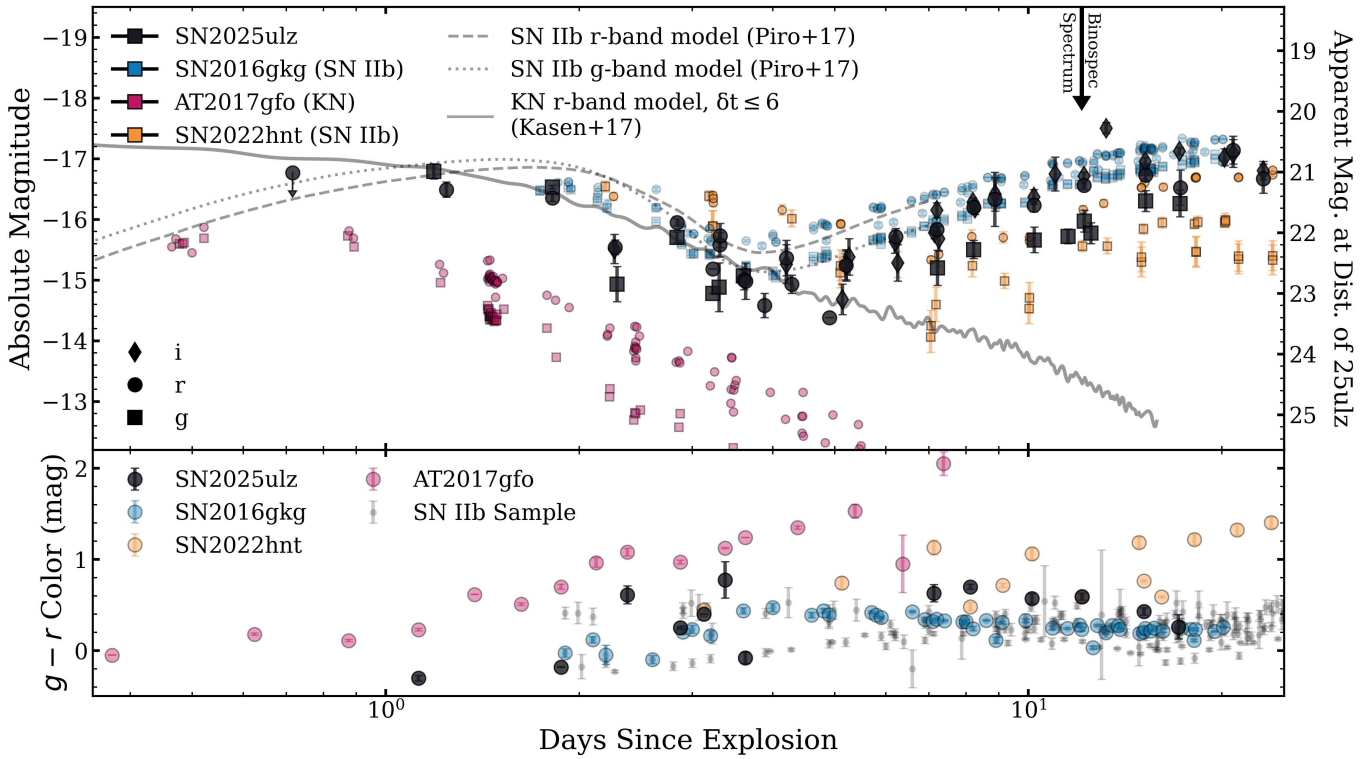

Figure 3. Top: A comparison of the *gri* light curves for SN 2025ulz (black), SN 2016gkg (blue; L. Tartaglia et al. 2017), SN 2022hnt (orange; J. R. Farah et al. 2025a), and AT 2017gfo (red; V. A. Villar et al. 2017). For SN 2025ulz, we choose an explosion date of MJD=60904 based on our shock-cooling modeling (see Section 4.2). The best-fit (i.e., lowest sum of the residual squared) *r*-band KN model (from D. Kasen et al. 2017) to SN 2025ulz for the early-time ($\delta t \leqslant 6$ days) light-curve decline is shown as a solid line. We also show the *r*- (black dashed line) and *g*-band (black dotted line) models for SN 2016gkg from A. L. Piro et al. (2017). At phase $\delta t \lesssim 6$ days all four observed light curves appear to redden as they fade rapidly at around the same rate. At $\delta t \gtrsim 6$ days, the light curves of SN 2025ulz and the other SNe IIb begin to rebrighten while the KN light curve continues to fade rapidly. Bottom: The $g - r$ color evolution of SN 2025ulz as compared to AT 2017gfo, SN 2016gkg, SN 2022hnt, and seven other SNe IIb (SN 1993J, M. W. Richmond et al. 1994; SN 2008ax, A. Pastorello et al. 2008; SN 2011dh, I. Arcavi et al. 2011; SN 2011ei, D. Milisavljevic et al. 2013; SN 2011fu, A. Morales-Garoffolo et al. 2015; SN 2013df, A. Morales-Garoffolo et al. 2014; SN 2024uwq, B. M. Subrayan et al. 2025). The color evolution of SN 2025ulz is very similar to the rest of the SNe IIb population.

Program (STEP) pipeline, as described in A. Santos et al. (2024). We report detections and 3σ upper limits on our T80S observations using a methodology similar to our SOAR imaging.

The *gri* light curve of SN 2025ulz is shown in Figure 3, with both our photometry and publicly available photometry. Our other observations are used for modeling and are provided in Table 4.

3.3. Optical Spectra

We observed SN 2025ulz and its host galaxy SDSS J155154.16 +305409.3 starting on 2025 August 21 with the Low-Resolution Imaging Spectrograph (J. B. Oke et al. 1995) on the Keck I telescope located on Maunakea, Hawaii, USA. We observed with the 400/3400 grism on the blue side and 400/8500 grating on the red side in conjunction with the d560 dichroic and the 1.″0 long slit, covering a continuous wavelength range of approximately 3000–10500 Å. In this mode, we observed for 5×930 s and 5×900 s on the blue and red arms, respectively, although we cut the final blue exposure to 628 s and red exposure to 646.6 s due to poor atmospheric transparency. We processed all spectra using `PypeIt` (J. X. Prochaska et al. 2020a, 2020b), calibrating the science spectra with dome flat exposures and obtaining a wavelength solution with arc lamp exposures obtained on the same night and instrumental configuration. We extracted a one-dimensional spectrum located around the position of the host galaxy and performed flux calibration with a spectrum of BD +33d2642 obtained on the same night, with telluric corrections derived from atmospheric grids of Maunakea. We then scale the continuum flux to the Pan-STARRS photometry, which scales the line flux appropriately.

Additionally, we observed SN 2025ulz on 2025 August 30 ($\delta t \sim 12$ days postdiscovery) using Binospec on MMT. This spectrum was taken with an exposure time of 5×900 s using a 1.″0 slit and the 270 lines/mm grating centered at 6800 Å for a total wavelength range of roughly 3800–9200 Å. This spectrum was triggered using the `PyMMT` package (M. Shrestha et al. 2024) as part of the Searches After Gravitational waves Using ARizona Observatories program (SAGUARO; M. J. Lundquist et al. 2019; K. Paterson et al. 2021; J. C. Rastinejad et al. 2022; G. Hosseinzadeh et al. 2024). Processing of the two-dimensional Binospec spectrum, including flat-fielding, sky subtraction, and wavelength and flux calibration, were done using the Binospec IDL pipeline (J. Kansky et al. 2019). The one-dimensional spectrum was then extracted using standard IRAF techniques (D. Tody 1986, 1993). A careful telluric correction was performed using the IRAF `telluric`[35] task, by creating an atmospheric model using the standard star (G191-B2B). We removed the intrinsic stellar features from the standard and the resulting telluric model was scaled, wavelength-shifted and

[35] https://iraf.readthedocs.io/en/doc-autoupdate/tasks/noao/imred/specred/telluric.html

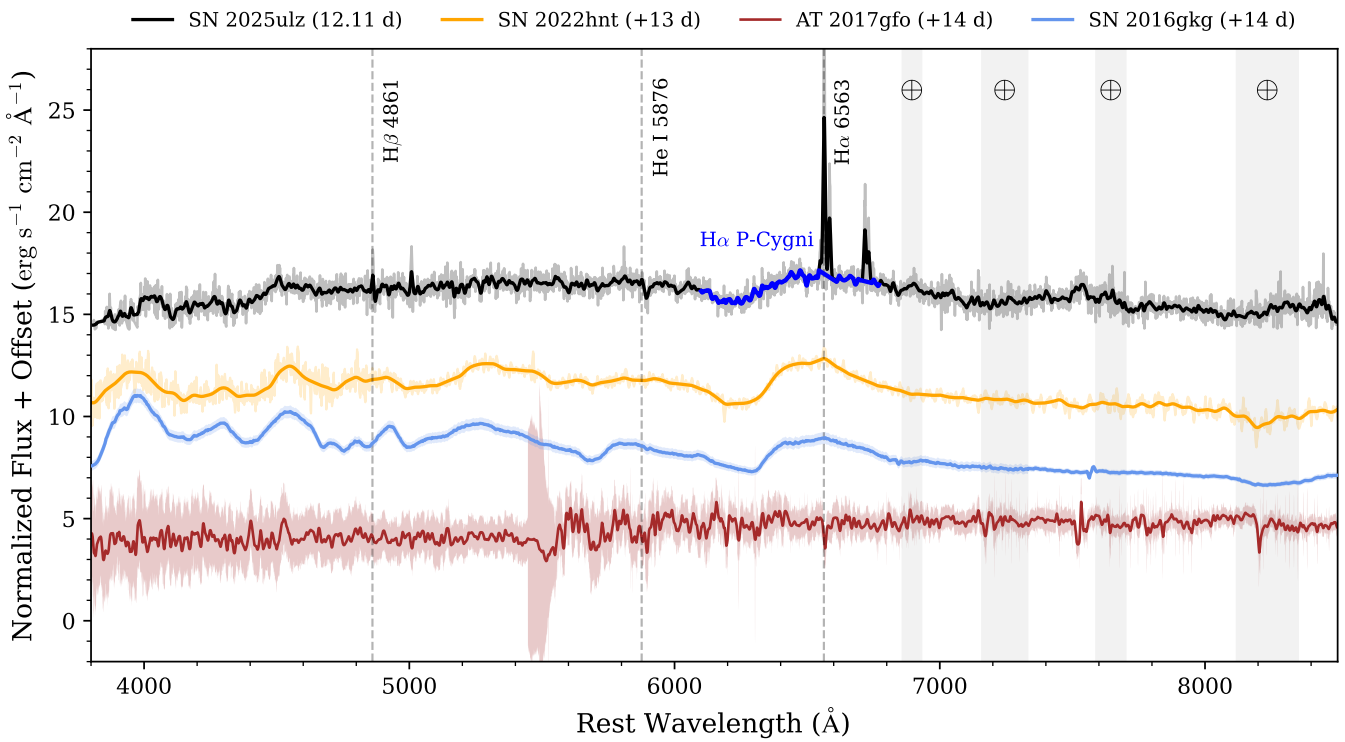

Figure 4. Comparison of the MMT optical spectrum of SN 2025ulz (black) to the type IIb SN 2022hnt (orange; J. R. Farah et al. 2025a), SN 2016gkg (sky blue; L. Tartaglia et al. 2017), and the KN AT 2017gfo (red; E. Pian et al. 2017), all at similar phases. The low opacity colored regions behind the spectra show the 1σ uncertainty and the gray vertical strips are regions of telluric features. The spectral features from SN 2025ulz appear most similar to SN 2022hnt and do not show any similarity with AT 2017gfo. Most notably, the broad P-Cygni Hα feature highlighted in dark blue, present in both SN 2025ulz and SN 2022hnt, is not expected, nor seen, in the KN spectrum.

divided to get the telluric corrected science spectrum (N. Rudolf et al. 2016). The reduced Binospec spectrum is shown in Figure 4, alongside similar phase spectra of the type IIb SN 2022hnt (J. R. Farah et al. 2025a), SN 2016gkg (L. Tartaglia et al. 2017), and the KN AT 2017gfo (E. Pian et al. 2017).

3.4. Radio Observations

On 2025 August 26, we observed SN 2025ulz with the upgraded Giant Metrewave Radio Telescope under program 48_120 (PI: Laskar). Observations were taken using the band 5 receiver ($\nu \approx 1.26$ GHz) with a total observation length of 106 minutes. We used 3C286 and J1609+266 as the flux and phase calibrators, respectively. The data were reduced and imaged using standard practices in the Common Astronomy Software Applications version 6.5.4 (CASAv6.5.4; J. P. McMullin et al. 2007; Team CASA et al. 2022), including two rounds of self-calibration. This observation had a beam size of $\sim 2\farcs5$ and an rms error of ~ 27 μJy, and no evidence of emission at the location of SN 2025ulz.

We observed SN 2025ulz with the Very Large Array (VLA) over two epochs on 2025 August 22 and 30 (VLA configuration B→C) under program 22A-417 (PI: Alexander). The first epoch spanned 1 hr and was at *C* band ($\nu \approx 6$ GHz). In the first epoch, 3C48 and J1602+3326 were used as the flux and phase calibrators, respectively. The second epoch spanned 2 hr and was at *S*, *C*, and *X* bands ($\nu \approx 3, 6, 10$ GHz, respectively). During the second epoch, 3C286 and J1602 +3326 were used as the flux and phase calibrators, respectively. All data were reduced and imaged using standard practices in CASAv6.5.4. All epochs had a beam size of $\sim 0\farcs5$–$1\farcs5$ and the image rms was $\sim$(6–10) μJy, with no evidence of emission.

SN 2025ulz was observed for three epochs using shared time on the South African MeerKAT radio telescope from programs MKT-24113/MKT-24127/MKT-24270 (PI: Bruni/Alexander/Mooley; triggered by PI Bruni under MKT-24113) on 2025 August 21 and 28 and 2025 September 13. The first two epochs used the MeerKAT S-band receiver ($\nu \approx 3$ GHz) and the third epoch used the *UHF*-, *L*-, and *S*-band receivers ($\nu \approx 0.81$, 1.28, 3 GHz, respectively). The MeerKAT observations were reduced and imaged by the South African Radio Astronomy Observatory pipeline. This resulted in a detection of diffuse resolved (i.e., larger than the synthesized beam size) emission consistent with the location of the transient host galaxy, with a major beam size of $\sim 5''$–$20''$ (although the beam is highly elongated, e.g., Table 5) and an image rms $\sim$(4–45) μJy beam^{-1}. Note that we know that the emission must be mostly diffuse because it is not detected in the deeper, higher-resolution radio images from the VLA, indicating that the emission is resolved out. Given the previous disagreement about the transient nature of the flux density measured from these observations (G. Bruni et al. 2025b, 2025c, 2025d; L. Rhodes et al. 2025), we re-extract a flux from the images using both a two-dimensional Gaussian fixed to the size of the beam and a two-dimensional Gaussian with a variable size. We then convert all flux density values to units of μJy/beam and find $F_\nu \approx 59$–$185\,\mu$Jy beam^{-1} that is dependent only on the frequency of the observation, not the time. Therefore, regardless of the fitting method used, the detections are consistent within 1σ with nonvarying emission.

We observed SN 2025ulz with the Northern Extended Millimetre Array (NOEMA) 3mm receiver under program

S25CS (PI: Laskar) on 2025 August 22. The observation used 3C345 and J1600+335 as the flux and phase calibrator, respectively. The data were reduced in GILDAS,[36] following standard calibration procedures, and imaged using CASAv6.5.4. This resulted in a beam size of $\sim 3''$–$4''$, an image rms of ~ 21 μJy, and no evidence of emission.

Finally, we observed SN 2025ulz at 225.5 GHz with the Submillimeter Array (SMA) on 2025 August 21 under the Pursuit of Extragalactic Transients with the SMA program (PI: Berger). The data were reduced and imaged using the Calibrator Observations for Measuring the Performance of Array Sensitivity and Stability (COMPASS) pipeline resulting in an rms of 250μJy, a beam size of $\sim 3''$, and no evidence of emission.

We do not detect any radio emission from SN 2025ulz, and we are confident that the diffuse emission detected by MeerKAT is from the host galaxy rather than the transient (also see Section 4.4). For flux and limit extraction from all radio data (except those from the SMA, for which we use COMPASS), we fit a two-dimensional Gaussian fixed to the synthesized beam size using the CASA task `imfit` at the location of SN 2025ulz. All limits are three times the rms noise in a nearby empty portion of the sky. Our radio observations are summarized in Table 5.

4. Analysis and Discussion of SN 2025ulz

4.1. The Light Curve and Spectrum are Consistent with SNe IIb

Figure 3 shows the *gri* optical light curve of SN 2025ulz compared to the *gr* light curves of KN AT 2017gfo (V. A. Villar et al. 2017) and two SNe IIb: SN 2022hnt (J. R. Farah et al. 2025a) and SN 2016gkg (L. Tartaglia et al. 2017). For reference, we show the numerical model fits to SN 2016gkg from A. L. Piro et al. (2017). For SN 2025ulz, we include the *i* band to fill in the gaps and guide the eye because it evolves similarly to the *r*-band light curve. As shown in Figure 3, SN 2025ulz follows a similar photometric evolution to both SN 2016gkg and SN 2022hnt, with all three showing a reddening $\sim$2 days after explosion and a rebrightening $\sim$5–7 days after explosion. In addition, Figure 3 shows that, at all times, the $g - r$ color evolution of SN 2025ulz is comparable to that of other SNe IIb. Given that this rebrightening is inconsistent with KN models, the overall light curve of SN 2025ulz is more similar to that of an SN IIb than a KN.

Figure 4 shows the optical spectrum of SN 2025ulz from our MMT Binospec observation at phase $\sim$12 days postdiscovery. We also show optical spectra of SN 2022hnt (J. R. Farah et al. 2025a), SN 2016gkg (L. Tartaglia et al. 2017), and AT 2017gfo (E. Pian et al. 2017) for comparison. SN 2025ulz shows a broad P-Cygni Hα line, which we attribute to the SN, with a narrow Hα component, which we attribute to the host galaxy. SN 2022hnt shows a P-Cygni Hα line with an absorption component with a similar velocity ($v \sim 13{,}000$ km s^{-1}) to SN 2025ulz ($v \sim 15{,}600$ km s^{-1}) at a similar phase. In contrast, AT 2017gfo shows no strong spectral features at this phase, including a lack of any Hydrogen. Furthermore, KNe are relativistic transients with extremely fast outflows (dynamical ejecta velocities $v_{\rm ej} \sim (0.1$–$0.3)c$; D. Kasen et al. 2017), generally expected to be faster than the velocity of the hydrogen line in the SN 2025ulz spectrum. Therefore, based on the broad P-Cygni Hα line, the spectrum of SN 2025ulz is consistent with an SN IIb classification and inconsistent with a KN.

4.2. Modeling the Light Curve as a KN

For completeness, we attempt to fit the SN 2025ulz light curve as a conventional KN (i.e., AT 2017gfo-like) using the models from D. Kasen et al. (2017). The D. Kasen et al. (2017) model grid produces spectral evolution models for KNe spanning dynamical ejecta velocities $v_{\rm ej} \approx (0.03$–$0.4)c$, ejecta mass $M = (0.001$–$0.1)M_\odot$, and lanthanide fraction $X_{\rm lan} = 10^{-9}$–10^{-1}. We take their spectral model data and integrate the simulated spectrum convolved with the SDSS *r*-band transmission function to extract a simulated light curve for each model. For each model in their grid, we downsample the simulated light curve to our temporal coverage and compute the sum of the square residual ($\Sigma\epsilon^2$) with respect to our *r*-band light curve. We note that, since we are not interpolating over the D. Kasen et al. (2017) grid, this approach only produces approximations of the KN parameters. Exact KN parameters could be derived from a more detailed modeling of the SN 2025ulz light curve using existing Bayesian fitting codes (e.g., `MOSFiT`, J. Guillochon et al. 2018; `gwemopt`, M. W. Coughlin et al. 2018, 2019; `nmma`, P. T. H. Pang et al. 2023; `redback`N. Sarin et al. 2024), something that is out of the scope of this work.

We then find the best-fitting model for both the early light-curve decline ($\leqslant$6 days since explosion) and the entire light curve. The early light-curve fit has a low $\Sigma\epsilon^2 = 1.66$ and the full light-curve fit has a poor $\Sigma\epsilon^2 = 118.55$. As a result, in Figure 3 we show the best-fit model (lowest $\Sigma\epsilon^2$) for the early light curve as a solid line. This demonstrates that the early light curve can be fitted well with a conventional KN model, but not the full light curve. The early-time best-fit model has an ejecta mass of $M_{\rm ej} \approx 0.05\,M_\odot$, outflow velocity of $v_{\rm ej} \approx 0.2c$, and a lanthanide mass fraction $X_{\rm lan} \approx 10^{-2}$. In contrast, the best-fit model for the entire light curve, which is an extremely poor fit, has $M_{\rm ej} \approx 0.01\,M_\odot$, $v_{\rm ej} \approx 0.03c$, and $X_{\rm lan}10^{-9}$.

Based on this analysis, no model in the D. Kasen et al. (2017) grid is able to reproduce the luminosity of the second optical peak while simultaneously capturing the early-time light-curve features. This is expected given that the optical luminosity of the first peak requires a high $X_{\rm lan}$, while the optical luminosity of the second optical peak requires a small $X_{\rm lan}$ (D. Kasen et al. 2015). Furthermore, even though D. Kasen et al. (2015) predict a second peak in the *infrared*, we are not aware of any conventional KN model, irrespective of the viewing angle, that has a second *optical* light-curve peak more luminous than its initial peak (as is seen in SN 2025ulz).

We briefly consider, and subsequently disfavor, more extreme and irregular KN models. One model for GW signals from a subsolar-mass BNS merger is the fragmentation of a collapsar disk into multiple, low-mass NSs that later merge (B. D. Metzger et al. 2024; Y.-X. Chen & B. D. Metzger 2025). Under this model, we would expect an SN followed by multiple GW signals, with the last signal consistent with an NSBH/BNS merger (almost certainly with a chirp mass $\gtrsim 1M_\odot$) that occurs $\sim$hours-days after the initial GW signal (B. D. Metzger et al. 2024). In the case of S250818k, there was only one (low significance) GW signal reported from its

[36] https://www.iram.fr/IRAMFR/GILDAS/

localization region (e.g., as was noted in J. H. Gillanders et al. 2025). However, it is possible, given the model parameters, that LVK only detected the strongest of the many predicted signals. While we cannot entirely rule out this model, we strongly disfavor it given the overwhelming observational similarities between SN 2025ulz and other prototypical SN IIb, making the SN explanation considerably more plausible.

Relatedly, the SN IIb SN 2025uso was discovered ∼2 days after S2501818k and is in the localization volume of the event (K. C. Chambers et al. 2025). Based on publicly available light-curve information, the explosion date of this event is roughly consistent with the S2501818k merger date ($\delta t \sim -1$ day, similar to our computed explosion date for SN 2025ulz). Under the B. D. Metzger et al. (2024) model for KN from SSM BNS mergers, SN 2025uso should be considered an equally likely candidate KN associated with S250818k. However, we rule this out for the same reasons as SN 2025ulz; the simpler, prototypical SN explanation is much more plausible.

Another possible KN model is an extreme eccentric encounter between an NS and a BH. Under this model, the NS initially approaches on an orbit grazing the tidal radius of the BH and then on the next orbit is fully disrupted. This, in theory, can explain two electromagnetic flares (at the pericenter of both orbits) with only one GW signal (at the time of the full disruption of the NS; W. E. East et al. 2015). This model is rather unlikely because (1) it would require a very extreme initial orbit to explain the timescales of the two flares in the optical light curve; (2) the International Gravitational Wave Network (IGWN) alert had a ∼0% probability that this was an NSBH merger; (3) the *maximum* chirp mass is 0.87 $M_\odot$, indicating a hypothetical black hole mass $\lesssim 1 M_\odot$ and making this scenario extremely unlikely; and (4) it predicts the formation of an accretion disk, rather than the expanding outflow that is required to produce the P-Cygni Hα profile in our optical spectrum. Therefore, we also rule out this model.

4.3. Early Shock Cooling Light-curve Modeling

Shock cooling in type IIb SNe occurs when the explosion shock wave deposits energy into the progenitor's extended, partially stripped hydrogen envelope, which then radiates its residual thermal energy as it rapidly expands and cools in the subsequent hours to days following shock breakout (M. W. Richmond et al. 1994; S. E. Woosley et al. 1994; I. Arcavi et al. 2017a; N. Sapir & E. Waxman 2017). We fit the early ($\delta t \lesssim 7$ days since discovery) light-curve dataset of SN 2025ulz to semianalytic shock-cooling models described by N. Sapir & E. Waxman (2017), using a Markov Chain Monte Carlo (MCMC) routine implemented in the Light Curve Fitting package (G. Hosseinzadeh et al. 2024). We follow the same methods for the early shock-cooling light-curve modeling for type IIb as described in B. M. Subrayan et al. (2025). Two polytropic indices ($n = 3/2$ and $n = 3$) were considered to represent convective (red supergiant; RSG) and radiative (blue supergiant; BSG) progenitor envelopes. The MCMC simultaneously constrains the progenitor's radius (R), shock velocity (v_s), and envelope mass ($M_{\rm env}$), while an intrinsic scatter term (σ) scales the observational errors by $\sqrt{1+\sigma^2}$ to account for additional variance. A scaled ejecta mass parameter was also included but remains largely unconstrained due to its minimal impact on the early light curve. The best-fit models and the derived parameters for RSG and BSG progenitors are shown in Figure 5.

The early-time light curve of SN 2025ulz is well described by the semianalytic shock-cooling models of N. Sapir & E. Waxman (2017), with the inferred envelope mass $M_{\rm env}$ and progenitor radius R falling within the parameter space spanned by known type IIb events in the literature, as shown in Figure 6. The best-fit values of SN 2025ulz lie closest to SN 2022hnt and SN 2016gkg. This is also consistent with the spectral similarity between the two SNe at ∼+12 days (see Figure 4). The inferred $M_{\rm env}$ and R for SN 2025ulz also match the theoretical ranges predicted by S.-C. Yoon et al. (2017) and N. Sravan et al. (2020) for RSG progenitors with residual, thin hydrogen envelopes, typical of SN IIb that display P-Cygni H profiles in their spectra. We also note that the modeling yields an explosion epoch that consistently precedes the reported subthreshold GW event. However, this model can overestimate the rise time of the SN and may produce explosion epochs before the true explosion date (J. Pearson et al. 2023).

4.4. Host Galaxy Properties Reveal a Star-forming Galaxy

The star formation rate (SFR) of a host galaxy can provide important contextual information for the classification of transients. For example, due to the short lifetimes of their high mass progenitors, core-collapse SNe (CCSNe) are expected to occur at a higher rate in galaxies with active star formation. We use the results from `Blast`,[37] a web service and automated galaxy SED modeling software, to infer the physical properties of SN 2025ulz's host galaxy (D. O. Jones et al. 2024). For SN 2025ulz, `Blast` finds a stellar mass $M_* = 1.23^{+0.21}_{-0.15} \times 10^{10}\,M_\odot$, SFR $= 0.298^{+0.244}_{-0.143}\,M_\odot\ {\rm yr}^{-1}$, and a specific SFR sSFR $= 2.37^{+2.02}_{-1.19} \times 10^{-11}\,{\rm yr}^{-1}$. This SFR and host galaxy mass are consistent with the broader population of type IIb SNe (Y.-J. Qin & A. Zabludoff 2024; A. E. Nugent et al. 2025). We now explore other probes of SFR, including Hα, which probes star formation in the last 10 Myr, and the diffuse radio emission observed in MeerKAT, which probes the last 150 Myr (R. C. Kennicutt & N. J. Evans 2012).

Since no emission at the location of SN 2025ulz was visible in our Keck spectrum, we instead extracted a host galaxy spectrum. We first estimate the host extinction $E(B-V)$ using the Balmer decrement. We model both the Hα and Hβ lines with a Gaussian plus a linear continuum.[38] The model of Hα is shown in Figure 7. We integrate both the Hα and Hβ best-fit models to obtain the line flux. From the Hα/Hβ ratio, we find a host extinction of $E(B-V) \approx 0.49$ mag using the relations from A. Domínguez et al. (2013). This extinction is for the entire host galaxy and is likely overestimated along the line of sight to SN 2025ulz, since its location is outside the plane of the host galaxy and we do not detect Na ID in the MMT Binospec spectrum of the transient.

As a check on the `Blast` values, we compute the SFR and sSFR from Hα. By assuming a Milky Way $R_V = 3.1$, we correct the Hα line flux for both host and Milky Way dust extinction using the `extinction` Python package. We apply the relation from R. C. Kennicutt (1998) to obtain a host galaxy SFR $\approx 0.8 \pm 0.2\,M_\odot\ {\rm yr}^{-1}$, or sSFR $\approx 8 \times 10^{-11}\,{\rm yr}^{-1}$, from the H$\alpha$ line flux. This is consistent, but at the upper end of the uncertainty, with the SFR derived by `Blast`.

[37] https://blast.ncsa.illinois.edu/

[38] Additionally, we add a [N II] and [S II] Gaussian component to our Hα model.

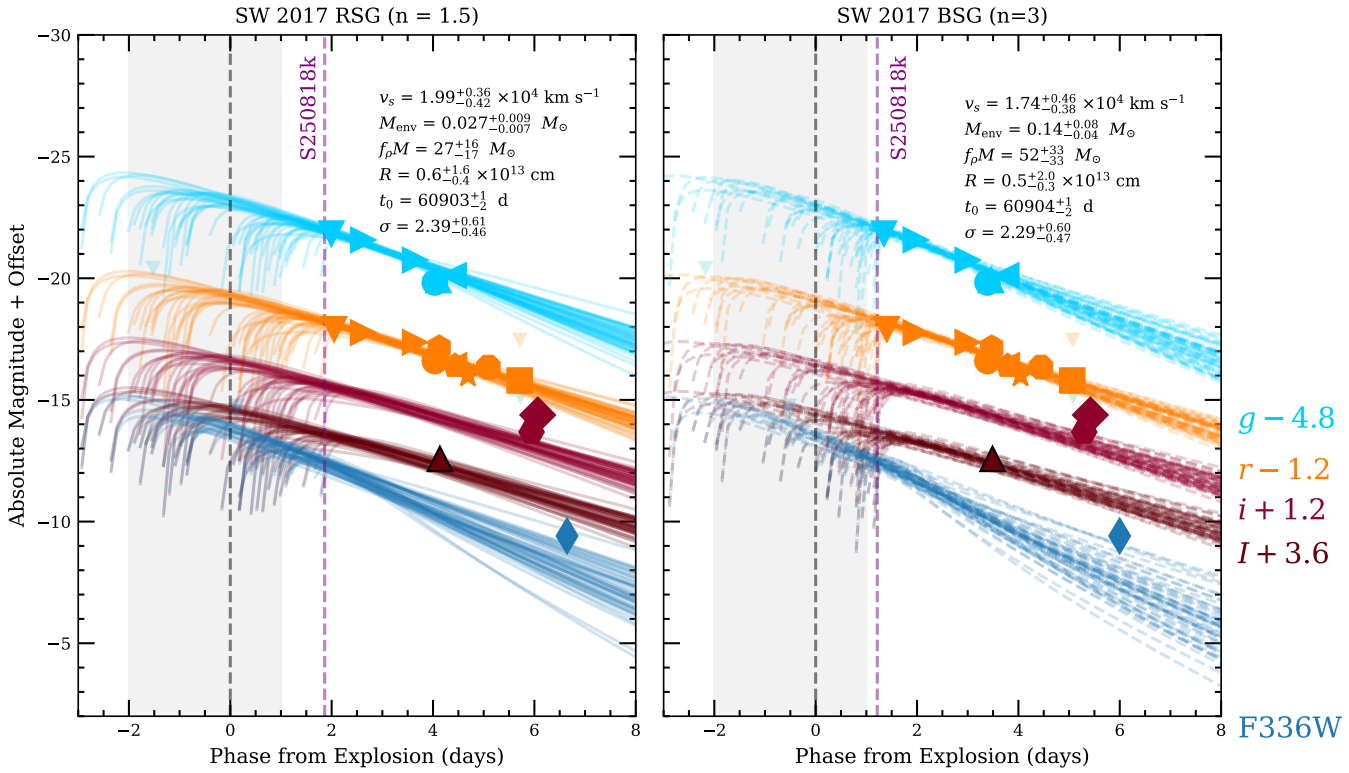

Figure 5. Fits of the *griI* and HST F336W (which is comparable to Swift/UVOT *U* band) light curves of SN 2025ulz with a shock-cooling modeling (N. Sapir & E. Waxman 2017), assuming two polytropic indices: $n = 3/2$ (left) and $n = 3$ (right). The best-fit explosion date, with uncertainties, and the detection date of S250818k are shown as gray and purple dashed lines, respectively.

The third epoch of MeerKAT observations was performed at the *UHF*, *L*, and *S* bands. This allows us to derive a spectral index for the diffuse emission of $\alpha \sim -0.9$, which is consistent with observations of star-forming galaxies (F. An et al. 2024). Using this spectral index and the relations from E. J. Murphy et al. (2011), we find SFR $\sim 5 M_\odot {\rm yr}^{-1}$. Given the ∼dex scatter in both relations used, and because the radio probes a longer epoch of star formation, the radio and Hα derived SFR are broadly consistent. This consistency is further evidence that the diffuse radio emission detected by MeerKAT is consistent with star formation in the past ∼150 Myr.

Qualitatively, the combined evidence from `Blast`, our radio observations, and our Hα measurements indicate a consistently high SFR over the past ∼100 Myr (∼1 $M_\odot$ yr^{-1}) for the host galaxy of SN 2025ulz. The SFRs computed here make the SN 2025ulz host consistent with the larger population of CCSN hosts presented in Y.-J. Qin & A. Zabludoff (2024), A. E. Nugent et al. (2025) but, alone, does not necessarily rule out a BNS origin (e.g., K. Belczynski et al. 2017).

4.5. The Radio Observations Rule Out a SGRB-like On-axis Jet

In contrast to the low-resolution (∼10″) MeerKAT observations, our higher-resolution (∼1″) GMRT, VLA, NOEMA, and SMA observations probe the existence of compact radio emission components. We do not detect radio emission at the transient position with any of these telescopes, and we show the light curve of the radio upper limits in Figure 8. For comparison, we show the radio data for AT 2017gfo, SN 2016gkg, and a sample of SGRBs from the literature.

These early-time radio upper limits on SN 2025ulz rule out an on-axis jet such as those seen in SGRBs, which would be expected for a face-on BNS merger (e.g., G. Schroeder et al. 2025a). However, our limits are still consistent with a BNS merger with an off-axis jet that only brightens in the radio after ∼10 days, like AT 2017gfo. Our radio limits are also consistent with the less luminous radio emission produced following a CCSN and, in particular, is consistent with the luminosity of the SN IIb 2016gkg (see Figure 8).

5. A Search for Additional Kilonovae Candidates

Given the overwhelming photometric and spectroscopic evidence that SN 2025ulz is a type IIb SNe and not a counterpart to S250818k, we search the TNS for other transients (1) with coordinates inside the 95% localization region for S250818k from the IGWN data stream and (2) reported within one week of the discovery of S250818k. This search reveals 121 electromagnetic candidate counterparts, one of which is SN 2025ulz. This suggests that the KN search after S250818k (and likely other GW events, see K. Ackley 2025) would have benefited from follow-up of additional candidates.

Expanding on the method in J. C. Rastinejad et al. (2022), we vet these candidates to determine the likelihood of association with S250818k. For each step in their vetting process, we develop a scoring algorithm that quantifies our confidence in the association of a transient with the GW event. Our scoring procedure consists of four components:

1. Score from the two-dimensional localization (Section 5.1).
2. Score from the distance localization (Section 5.2).
3. Score from comparison to known asteroids and point source/variability catalogs (Section 5.3).
4. Score from comparing the photometric evolution to models and existing observations (Section 5.4).

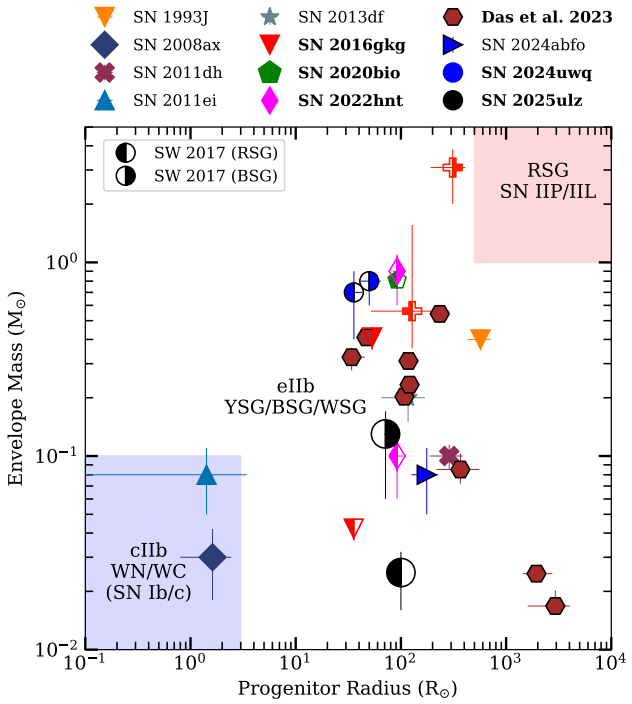

Figure 6. The shock-cooling model envelope mass versus progenitor radius for SN 2025ulz as compared to a population of SNe IIb. SN 2025ulz lies in a similar region of parameter space to the other SNe IIb and is in nearly the same region as SN 2016gkg using the same model. SNe highlighted in bold have values derived from similar shock-cooling modeling, while the others adopt values from alternate methods. Points with the right half-filled are from the N. Sapir & E. Waxman (2017) BSG model and points with the left half-filled are from the N. Sapir & E. Waxman (2017) RSG model. Published values for other SNe in this figure are obtained from: SN 1993J: S. E. Woosley et al. (1994), SN 2008ax: A. Pastorello et al. (2008), R. A. Chevalier & A. M. Soderberg (2010), SN 2011dh M. C. Bersten et al. (2012), SN 2011ei: D. Milisavljevic et al. (2013), SN 2011fu: A. Morales-Garoffolo et al. (2015), SN 2013df: A. Morales-Garoffolo et al. (2014), SN 2016gkg: I. Arcavi et al. (2017a), SN 2017jgh: P. Armstrong et al. (2021), SN 2020bio: C. Pellegrino et al. (2023), SN 2022hnt: J. R. Farah et al. (2025b), SN 2024uwq: B. M. Subrayan et al. (2025), SN 2024abfo: A. Reguitti et al. (2025), and K. K. Das et al. (2023).

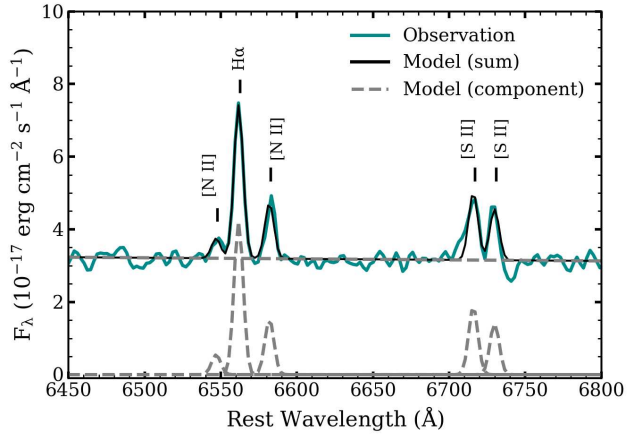

Figure 7. Model of our Keck spectrum that is dominated by emission from the SN 2025ulz host. We use this model to derive an SFR for the host galaxy for comparison with our radio derived SFR.

Finally, we take the resulting score from each of these components and multiply them to obtain a total score between 0 and 1, such that a higher score generally indicates a more probable candidate.

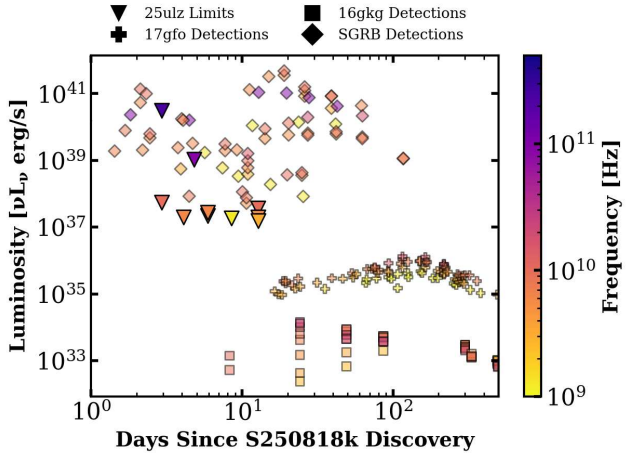

Figure 8. The radio light curves of SN 2025ulz (downward triangles as limits) as compared to SN 2016gkg (squares; N. A. J. et al. 2022), a sample of short SGRB radio detections (diamonds; E. Berger et al. 2005; A. M. Soderberg et al. 2006; A. J. Levan et al. 2009, 2024; W. Fong et al. 2014, 2015, 2021, 2025; A. J. Nayana & P. Chandra 2014; G. P. Lamb et al. 2019; W.-f. Fong et al. 2022; T. Laskar et al. 2022; L. Rhodes et al. 2023; G. E. Anderson et al. 2024; A. E. Nugent et al. 2024; G. Schroeder et al. 2024, 2025a, 2025b, 2025c; J. An et al. 2025b; D. Dimple et al. 2025; R. Ricci et al. 2025a, 2025c), and AT 2017gfo (plus signs; K. D. Alexander et al. 2017, 2018; G. Hallinan et al. 2017; S. Kim et al. 2017; D. Dobie et al. 2018; R. Margutti et al. 2018; K. P. Mooley et al. 2018a, 2018b, 2018c; L. Resmi et al. 2018; G. Ghirlanda et al. 2019; A. Hajela et al. 2019; E. Troja et al. 2019; J. W. Broderick et al. 2020; S. Makhathini et al. 2021). The color of the point is the representative frequency of the receiver used for the observation. Our radio limits on SN 2025ulz rule out an SGRB-like on-axis jet but do not rule out SN IIb-like or late-rising AT 2017gfo-like radio emission.

A summary of this scoring is shown in Figure 9 and details are presented in the following subsections. For reference, we validated this scoring algorithm against AT 2017gfo and found that it has a score of $S \approx 0.55$, depending on if we use the photometric redshift (from the best matching host, $S = 0.54$) or spectroscopic redshift ($S = 0.56$). This score of $\sim$0.55 for the known KN counterpart to a BNS merger suggests that a candidate need not have a score of $\sim$1 to be worth consideration.

5.1. Two-dimensional Localization Score

The IGWN localization map for GW events provides a probability density in each HEALPix tile describing the likelihood that the GW event originated from that tile. These probability densities are normalized such that integrating over the entire sky provides a localization probability of 1.0. We extract the probability density from the HEALPix tile where each candidate is located and perform a two-dimensional integration over the localization region with a higher probability density (L. P. Singer et al. 2016a, 2018b). This cumulative probability is the score that the GW event originated from the candidate coordinates,[39] and is the two-dimensional localization score (S_{2D}).

5.2. Distance Score

Deriving a distance score requires distances for both the GW signal and the candidate electromagnetic counterpart. The distance to the GW event is given as a function of localization tile, where each tile in the localization map has an associated

[39] Since we use the cumulative probability, the score is less dependent on the NSIDE property of the HEALPix map, as compared to using the probability density.

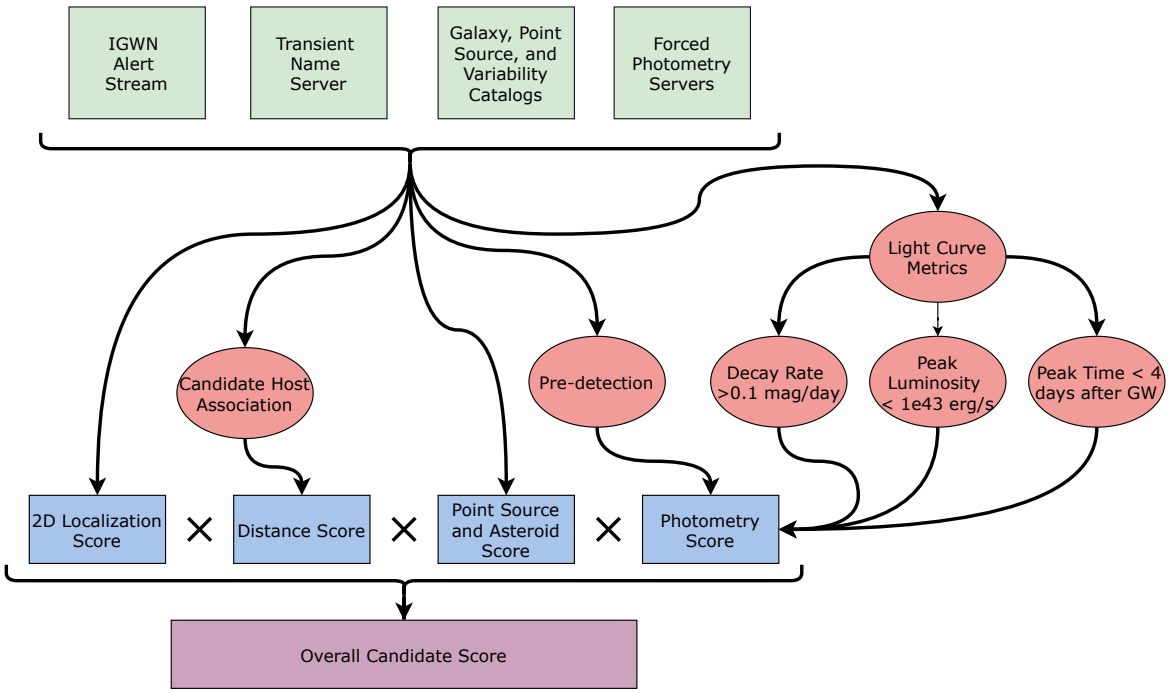

Figure 9. Flow diagram outlining our current candidate scoring algorithm. In general, it takes in IGWN alerts, TNS transients, various static catalogs, and forced photometry and derives multiple "subscores" from the data, eventually multiplying them together to obtain a total overall score for a candidate.

distance and uncertainty (L. P. Singer et al. 2016a, 2016b). We use the distance in the tile corresponding to the candidate coordinates as the distance to the GW event when computing the distance score for this candidate.

Finding the distance to the candidate is more difficult given that the redshift is typically not known. Therefore, we first query galaxy redshift catalogs[40] for all potential host galaxies within 2′ (≈150 kpc at 260 Mpc) of the candidate. Note that we expect this host galaxy search to be relatively complete at $z \leqslant 0.3$, the distance scale that is relevant for this work, because Legacy Survey Data Release 10 is >90% complete out to this redshift (C. Li et al. 2024). For each galaxy match found, we compute the probability of chance coincidence ($P_{\rm cc}$; J. S. Bloom et al. 2002). We select all galaxies with $P_{\rm cc} < 0.1$ as potentially associated with the candidate. If no galaxies have $P_{\rm cc} < 0.1$, we select the galaxy with the minimum $P_{\rm cc}$ as the most likely host.

After finding the most probable host galaxies for the candidate, we extract the redshift and uncertainties from the respective catalog. From this, we derive a distance probability distribution for each host galaxy. The distance score $S_{\rm dist}$ is then the integrated joint probability of the host distance distribution and the GW distance distribution, derived along the line of sight to the transient (see Equation (A4)). Since we apply this approach to all host galaxies potentially associated with a candidate, and since the photometric redshifts of these galaxies may have unknown systematic uncertainties, we downweight the distance score by selecting the highest score among all potential host galaxies for this candidate. More details on the method used for this calculation are given in Appendix A.

5.3. Minor Planet and Point Source Catalog Comparison

We perform a cone search on the All-Sky Automated Survey for Supernovae Variable Star catalog X (B. J. Shappee et al. 2014; C. T. Christy et al. 2023), Gaia Data Release 3 Variable Star catalog (Gaia Collaboration et al. 2023), and Pan-STARRS (PS1) Point Source catalog (R. Beck et al. 2021) for any targets within 2″ of the candidate. If a match is found, then it indicates, e.g., a flaring star rather than a KN, and we assign a point source score of $S_{\rm PS} = 0$. Otherwise, if no match is found in these catalogs, we assign $S_{\rm PS} = 1$.

We also pull the file of asteroid ephemerides from the Minor Planet Center (MPC).[41] Using simple two-body evolution around the Sun, we find all asteroids that are approximately within 10° of the candidate location at the time of the first photometric detection. For any asteroid found in this initial search, we perform a full n-body evolution to find the more precise location at the time of the first photometric detection of the candidate. This is implemented using the `kete` Python package (D. Dahlen et al. 2025). If a match is found within 25″ of the candidate, it receives an MPC score of $S_{\rm MPC} = 0$; otherwise, it receives a score $S_{\rm MPC} = 1$. $S_{\rm MPC} \times S_{\rm PS}$ is the final score for this portion of the analysis.

5.4. Photometry Scoring

We score candidates with available photometry by comparing basic metrics from their light-curve properties to both AT 2017gfo and KN models (see below). Throughout the photometry scoring, we choose a minimum score of 0.1. This, in effect, prevents a single photometric anomaly in the light curve from completely ruling out the candidate. This is a way

[40] These include Dark Energy Spectroscopic Instrument Early Data Release (DESI Collaboration et al. 2024), GLADE (G. Dálya et al. 2018), Gravitational Wave Galaxy Catalog (D. J. White et al. 2011), Hecate (K. Kovlakas et al. 2021), Legacy Survey Data Release 10 (R. Zhou et al. 2023), Pan-STARRS (PS1) Galaxy catalog (R. Beck et al. 2021), and Sloan Digital Sky Survey Data Release 12 photo-z catalog (S. Alam et al. 2015).

[41] https://www.minorplanetcenter.net/

Table 2
Top Candidate Scores and SN 2025ulz (Full Table in Appendix B)

TNS Name	R.A. (deg)	Decl. (deg)	Overall Score	Two-dimensional Score	Point Source Score	Distance Score	Peak Luminosity (erg s^{-1})	Time of Peak[a] (days)	Decay Rate[a] (mag day^{-1})	Predetection Score
AT2025usl	237.1445	32.2938	0.73	0.85	1.00	0.86	7.42×10^{41}	⋯	⋯	1
AT2025uuf	310.1678	64.6115	0.51	0.59	1.00	0.87	5.11×10^{41}	⋯	⋯	1
AT2025uus	244.2946	39.6485	0.41	0.97	1.00	0.42	9.88×10^{41}	⋯	⋯	1
AT2025uua	261.4404	51.9287	0.39	0.39	1.00	1.00	8.90×10^{41}	⋯	⋯	1
AT2025uow	53.3796	−30.0963	0.38	0.45	1.00	0.87	2.38×10^{42}	0.05	0.13	1
AT2025usk	241.2050	35.7908	0.35	0.99	1.00	0.35	1.04×10^{42}	⋯	⋯	1
AT2025uvu	236.7145	29.9994	0.31	0.76	1.00	0.42	5.68×10^{41}	⋯	⋯	1
AT2025wfs	236.5714	31.8389	0.30	0.83	1.00	0.36	3.44×10^{41}	⋯	⋯	1
AT2025uxu	270.6914	56.4917	0.24	0.30	1.00	0.80	4.97×10^{41}	0.16	0.25	1
AT2025uut	283.5697	60.0326	0.15	0.52	1.00	0.29	6.85×10^{41}	⋯	⋯	1
AT2025utu	301.9844	61.3465	0.15	0.25	1.00	0.63	6.34×10^{41}	0.37	0.33	1
AT2025usn	237.6131	30.3337	0.12	0.64	1.00	0.20	1.04×10^{42}	⋯	⋯	1
AT2025uuc	264.9940	53.3377	0.10	0.35	1.00	0.30	8.79×10^{41}	⋯	⋯	1
AT2025uog	58.3270	−33.1844	0.09	0.52	1.00	0.18	1.60×10^{42}	0.05	0.20	1
AT2025uul	237.0139	29.7992	0.09	0.64	1.00	0.15	7.60×10^{41}	⋯	⋯	1
AT2025uur	236.7506	30.5273	0.09	0.81	1.00	0.12	6.46×10^{41}	⋯	⋯	1
AT2025uzu	244.2891	41.7935	0.09	0.53	1.00	0.17	7.50×10^{41}	0.14	0.12	1
AT2025unm	247.0348	42.0573	0.08	0.91	1.00	0.95	4.94×10^{41}	0.12	0.02	1
⋮					⋮					⋮
SN 2025ulz	237.9758	30.9024	0.00	0.66	1.00	0.68	2.12×10^{42}	26.76	3.07	1

Note.
[a] The empty row indicates that there was only one public photometry point, which is not enough to fit the light curve and compute this value. We therefore do not consider a score from this value when computing the total score.

to "soften" the effects of the assumption that all KNe look like the existing models.

We first check for predetections in the ATLAS forced photometry for the 181 days prior to GW event S250818k. We only consider 5σ detections with at least two other 5σ detections within the range ± 5 days. If any predetections are discovered, we assign a score of $S_{\rm pre} = 0.1$, otherwise $S_{\rm pre} = 1$.

For candidates with more than one detection after the GW discovery date, we also compare the rise time, decay rate, and peak luminosity to KNe models. To extract these properties from the candidate light curves we first gather all optical photometry in the g, r, i, ATLAS-c, or ATLAS-o filters.[42] We then fit the light curve with both a power law and a broken power law. We only fit a broken power law to the data if more than five photometric detections are available; otherwise, the model does not have enough constraining power.

After fitting both models to the photometry, we choose the model with the lowest Akaike information criterion (AIC).[43] From the light-curve model, we derive a decay rate and a rise time. KN models show that, in all cases, the light curve should decay at a rate faster than 0.1 mag day^{-1} (e.g., D. Kasen et al. 2015, 2017; C. D. Kilpatrick et al. 2021; J. C. Rastinejad et al. 2022). Therefore, for any decay rate <0.1 mag day^{-1}, we assign a decay rate score of $S_{\rm DR} = 0.1$, otherwise $S_{\rm DR} = 1$. Similarly, no KN models have a rise time greater than 4 days long (e.g., D. Kasen et al. 2015, 2017; C. D. Kilpatrick et al. 2021; J. C. Rastinejad et al. 2022). We therefore require the peak of the light curve to occur less than 4 days after the GW event. If the peak occurs after 4 days the candidate receives a score $S_{\rm RT} = 0.1$, otherwise $S_{\rm RT} = 1$.

Finally, we also compute the maximum luminosity using the maximum observed flux in the light curve (not the maximum flux of the model) at the distance to the GW event along the line of sight to the candidate. Since the maximum mass of an NS sets an upper limit on the maximum outflow mass, we can conservatively assume that a KN should not have a luminosity $\nu L_\nu > 10^{43}\,{\rm erg\,s^{-1}}$ (e.g., D. Kasen et al. 2015, 2017; C. D. Kilpatrick et al. 2021; J. C. Rastinejad et al. 2022). Any candidate with $\nu L_\nu > 10^{43}\,{\rm erg\,s^{-1}}$ receives a score $S_L = 0.1$, otherwise $S_L = 1$. To obtain a final photometry score, we multiply all of the previously discussed photometry subscores to obtain $S_P = S_{\rm PD} \times S_{\rm DR} \times S_{\rm RT} \times S_L$.

5.5. Application to S250818k

In the case of the BNS GW event S250818k, we find 121 candidates with the scores summarized in Table 2 (the full score information is given in Table 3). The locations of these candidates with respect to the GW localization map are shown in Figure 1. SN 2025ulz receives a score of S ≈ 0.0011 as a result of both its distance ($S_{\rm dist} \approx 0.16$) and photometric evolution ($S_{\rm phot} \approx 0.01$). We discuss SN 2025ulz in more detail in Section 5.6.

We briefly discuss the other high scoring candidates given in Table 2. In total, $41/121 \approx 34\%$ of the candidates have a score $S \geqslant 0.01$ and, of those 41, only 18 have more than one photometry point. We visually inspect these 18 transients to identify a subset of interest to discuss in more detail. In particular, we ignore candidates with poor host association (i.e., the host used for the distance score is clearly not related

[42] Since we are trying to derive the properties of the bulk evolution of the light curve, it is safe to assume that these evolve relatively similarly.
[43] The AIC score takes the model's complexity into account for model comparison to help ensure we are not overfitting. We also tried the Bayesian information criterion and it did not make a difference.

to the transient position, e.g., AT 2025utu), the best matching host galaxy has a distance >1000 Mpc (e.g., AT 2025uog),[44] and/or those that have multiple photometry points but all in different filters (e.g., AT 2025vag). We find two promising candidates, AT 2025uow (J. Tonry et al. 2025) and AT 2025uxu (A. Salgundi 2025), but none with enough information to unambiguously prove whether or not they are KNe, suggesting that a more comprehensive follow-up strategy of transients found in the localization volume of a GW event would be beneficial for the community. The light curves of both of these candidates are given in Figure 10.

AT 2025uow has a total score of 0.38, mostly due to its $S_{2D} = 0.45$. The light curve reveals a rapid decline at a rate of 0.13 mag day^{-1}, a red color (based off of only one epoch with an ATLAS-*c* and ATLAS-*o* filter observation within 1 day of each other), and a peak luminosity $\nu L_\nu \approx 2 \times 10^{42}$ erg s^{-1}. All three of these photometric properties are consistent with KNe models. However, there is one significant ATLAS predetection at $\delta t \approx -2$ days. Based on this predetection, the light curve appears to *peak*, rather than begin to rise, near the discovery of S250818k, making it unlikely that this is a KN associated with a BNS merger.

AT 2025uxu has a score of 0.24, primarily because of its two-dimensional localization score of 0.3, and only two photometric detections in the ZTF *g* band following the discovery of S250818k. These two detections fade at a rate of ∼0.25 mag day^{-1} and have a peak luminosity $\nu L_\nu \approx 5 \times 10^{41}$ erg s^{-1}, both consistent with KNe models. However, we have no color information and the ATLAS upper limits from before the discovery of S250818k are nonconstraining. Therefore, given this lack of information, we hesitate to draw any conclusions for this object.

J. H. Gillanders et al. (2025) finds seven other candidates associated with S250818k, all of which they rule out. Based on our algorithm, six of these candidates, with the exception of AT 2025uuf, receive a score $S \approx 0$ (Table 3). AT 2025uuf has the second highest score ($S = 0.51$) of all of our candidates. However, only the Pan-STARRS photometry reported to TNS is publicly available, and the ATLAS limits are nonconstraining based on the Pan-STARRS detection. Therefore, we defer to the conclusion of J. H. Gillanders et al. (2025) that AT 2025uuf is inconsistent with a KN.

5.6. Temporal Evolution of the SN 2025ulz Score

The public GCNs for the follow-up of SN 2025ulz provide a unique opportunity to apply this scoring algorithm as a function of time. In this way, we can demonstrate how the score changes as more information is found on the transient. To do this we account for:

1. The release of new IGWN alerts with updated skymaps. This affects both the two-dimensional score and distance score.
2. The measurement of a spectroscopic redshift by V. Karambelkar et al. (2025) of SN 2025ulz at ∼2.6 days after the discovery of the GW event. This affects the distance score.

[44] The transients that fall into this category typically lie in a HEALPix tile with an unusually high distance uncertainty and have a photometric distance with an unusually high uncertainty. This combination results in the transient not being ruled out by its distance during the automated scoring.

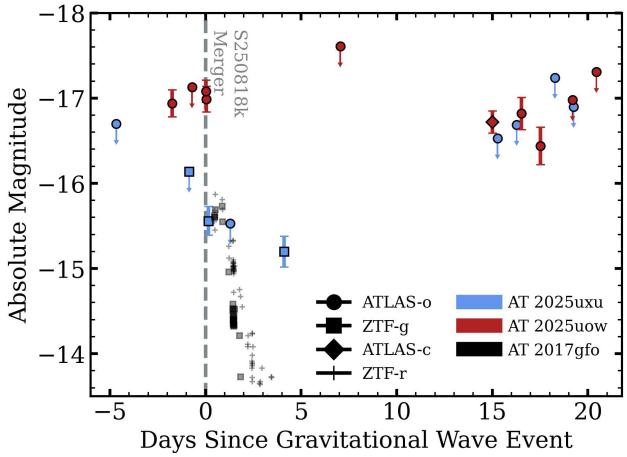

Figure 10. Light curves of the publicly available data from ATLAS and TNS on AT 2025uxu (blue) and AT 2025uow (red) as compared to AT 2017gfo (black; V. A. Villar et al. 2017). We scale the observed magnitudes of AT 2025uxu and AT 2025uow to the mean distance in the corresponding HEALPix tile in the localization map of S250818k. The merger date associated with S250818k is shown as a gray dashed vertical line. Different markers indicate different telescope filters.

3. The announcements of new photometric measurements of SN 2025ulz. We do this by fitting the data binned in one day increments. Note that we do not include the Pan-STARRS light curve from J. H. Gillanders et al. (2025) because it was not made public until after the time period considered here.

The minor planet and point source scores are held constant at $S_{PS} = S_{MPC} = 1$ since SN 2025ulz is not found to spatially coincide with any known point sources or asteroids.

In the bottom panel of Figure 11, we show the evolution of the two-dimensional, distance, photometry, and total score. In the top panel, we show the evolution of the light-curve models used for extracting the photometry score. The distance score is strongly affected by the measurement of a spectroscopic redshift because the scoring algorithm switches from using a photometric redshift with large, asymmetric uncertainties to a spectroscopic redshift with small uncertainties, which we set to $\delta z = 10^{-3}$. This, in effect, treats the spectroscopic redshift distance measurement as a delta function, lowering the distance score from $S_{dist} = 0.71 \rightarrow 0.16$.

The photometry score for SN 2025ulz is initially very high with a score $S_P = 1$. This is because the light curve of SN 2025ulz initially fades quickly and peaks soon after the GW discovery date, as is expected for a KN. However, after the observations on day 6, the score drops to $S_P = 0.1$ because, after we include the day 6 photometry, the AIC score for the broken power law drops below the single power-law score, indicating a better fit. This indicates that the light curve has begun to rise again and the decay rate score drops to $S_{DR} = 0.1$. At day 10 the photometry score drops again because the most recent photometry point is now more luminous than the first observation. This changes the time of peak to 10 days after the GW discovery, outside our conservative range of 0–4 days, and also drops the rise time score to $S_{RT} = 0.1$.

In Figure 12 we show the evolution of the SN 2025ulz score compared to the other candidates, and we show the number of candidates with a score greater than SN 2025ulz as a function

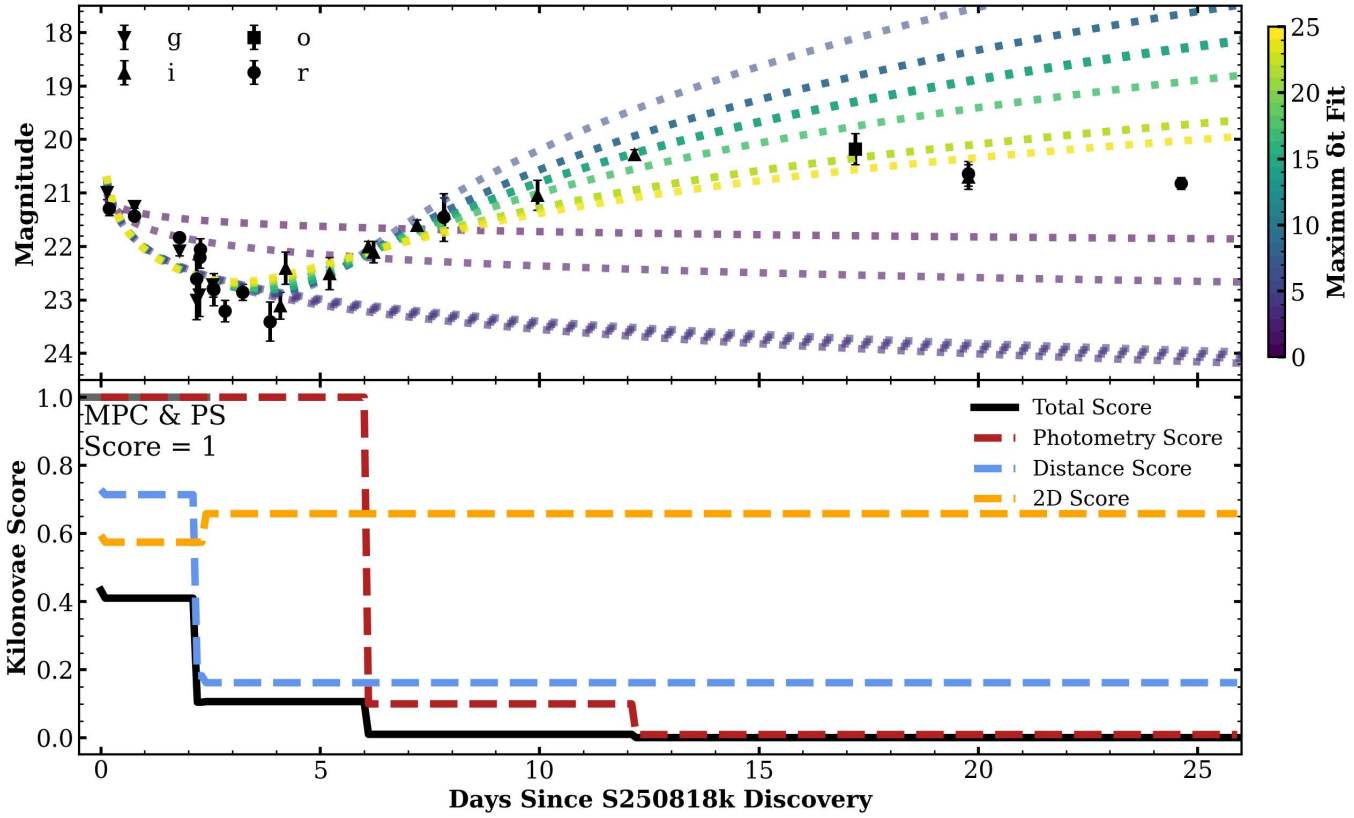

Figure 11. Top: The best-fit light curve after including different ranges of data. The color of the line represents the maximum δt days since discovery that was used when selecting data to fit. Bottom: The change in total score (red), photometry score (blue), distance score (black), and two-dimensional score (orange) over time as we include additional information/measurements of SN 2025ulz. The distance score drops after a spectroscopic redshift is measured at $\delta t \approx 2.6$ days. After the light curve turns over, the photometry score drops, since this turnover is inconsistent with KN models and the AT 2017gfo light curve.

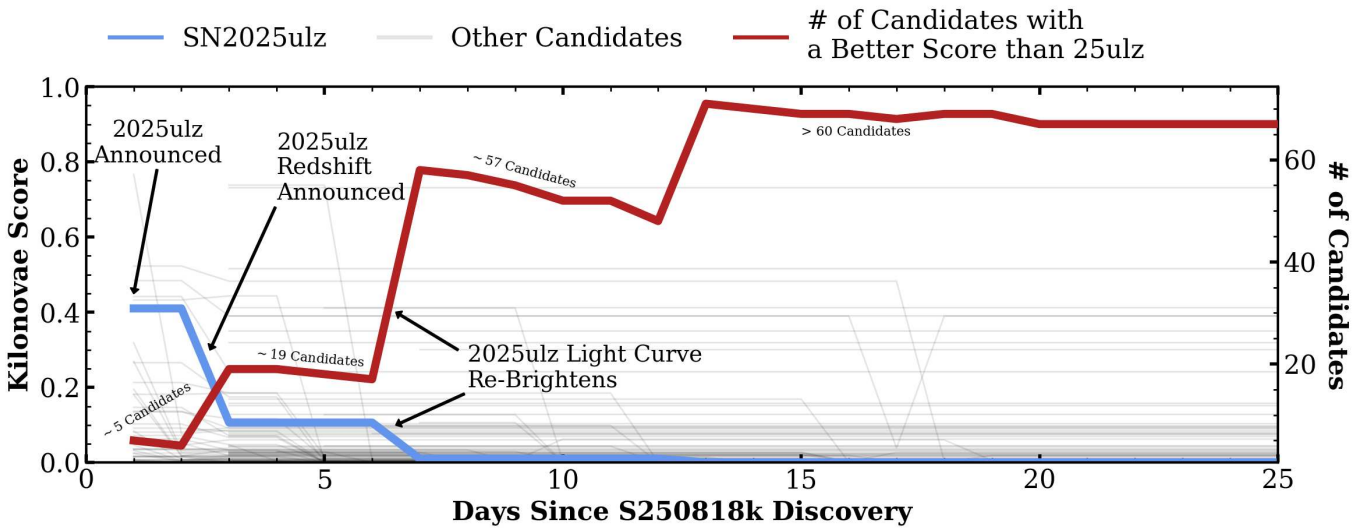

Figure 12. The evolution of the SN 2025ulz score (blue) as compared to the evolution of the scores of the rest of our candidates (gray). The red line shows the number of candidates with a better score than SN 2025ulz over time (right y-axis). The labels near the red line are the number of candidates with a score greater than SN 2025ulz at that time.

of time. At the time SN 2025ulz was announced, there were five transients discovered with a marginally higher score than SN 2025ulz, suggesting that additional candidates were also initially consistent with a KN and would have benefited from additional follow-up. The SN 2025ulz score drops as more observations are included, and thus more candidates have a higher score than SN 2025ulz. This increase in the number of candidates with a higher score than SN 2025ulz over time is likely caused by the lack of follow-up for these candidates, most of which are surely not KNe. With a more comprehensive

follow-up strategy of multiple promising candidates, the astronomical community could have continuously updated the list of promising KN candidates until each was ruled out or the true counterpart was found. Applying a similar algorithm, in real time, during future KN searches will assist with the community coordination of a comprehensive follow-up strategy.

6. Summary and Conclusions

On 2025 August 20, the LVK collaboration announced the discovery of S250818k, a GW event with a 29% probability of being a BNS merger and a 71% probability of being terrestrial. Soon after, the transient SN 2025ulz was discovered at the 66% localization contour of S250818k. This prompted follow-up observations across the electromagnetic spectrum to determine if SN 2025ulz was consistent with KN emission following the potential BNS merger.

In this Letter, we present and analyze observations of SN 2025ulz spanning from the ultraviolet to radio wavelengths. We also compare these observations against a novel scoring algorithm to determine the likelihood that a specific transient is associated with a BNS merger GW signal. Based on these observations, we find SN 2025ulz to be consistent with a SN IIb, and inconsistent with both KN models and the KN AT 2017gfo. A summary of our findings follows:

1. In the first $\sim$5 days after the discovery of S250818k, SN 2025ulz faded rapidly and reddened as it faded in the optical (Figure 3). This is both consistent with the broader population of SN IIb and reminiscent of AT 2017gfo. However, starting $\sim$6 days after the discovery of S250818k, the SN 2025ulz optical light curve begins to rebrighten, eventually reaching a peak luminosity at $\gtrsim$25 days. This optical rebrightening to a more luminous second peak is consistent with an SN IIb and inconsistent with both AT 2017gfo and KN models.
2. At $\delta t \sim 2.6$ days after discovery, we find that SN 2025ulz has a combined score of $S \sim 0.45$ (Figure 11). After the measurement of the spectroscopic redshift at $\delta t \approx 2.6$ days, this score drops to $S \sim 0.16$ because the spectroscopic redshift puts the distance $\sim 1.7\sigma$ above the best-fit GW distance along that line of sight.
3. By applying our photometry scoring algorithm to SN 2025ulz over time, we find that the early ($\delta t < 5$ days) optical light-curve evolution is consistent with KN models. But, similar to our qualitative discussion above, as soon as the optical light curve begins to rebrighten around $\delta t \sim 6$ days, it is no longer consistent with a KN, and the score drops (Figure 11).
4. Modeling of the initial decline in the SN 2025ulz light curve shows that it is consistent with the shock cooling expected from a SN IIb (Figure 5). Additionally, the envelope mass and progenitor radius derived from this model are consistent with the rest of the SN IIb population, and most similar to SN 2016gkg (Figure 6).
5. The optical spectrum of SN 2025ulz (Figure 4) has a broad P-Cygni Hα line with a velocity of $\sim$15,600 km s^{-1}. The strength and velocity of this Hα line is consistent with both the SN IIb SN 2022hnt and SN 2016gkg at nearly the same phase. If SN 2025ulz were a KN, we would expect a featureless spectrum, like AT 2017gfo, and a higher outflow velocity than measured from the Hα line.
6. We find no evidence for transient radio emission originating from SN 2025ulz (Figure 8). Our radio limits rule out an on-axis jet, like those seen in SGRBs, as would be expected for a face-on KN. Our radio observations do not rule out an off-axis KN, such as AT 2017gfo, or an SN IIb, such as SN 2016gkg.
7. We derive an SFR from the host Hα emission and diffuse radio emission from the MeerKAT observations. Both are consistent with SFR $\sim 1\ M_{\odot}\ \mathrm{yr}^{-1}$, indicating that the host galaxy is actively star forming. This finding is consistent with the CCSN interpretation of SN 2025ulz.

When this abundance of evidence is considered in its entirety, we find that an SN IIb is the most favorable interpretation of SN 2025ulz. Given this, we also apply our scoring algorithm to the 120 other transients reported to the TNS that are within the 95% region of the S250818k contour map. By doing this KN search, we find (1) 4–5 candidates more promising than SN 2025ulz at $\delta t < 2.6$ days (when the redshift was measured); (2) 19 candidates more promising than SN 2025ulz at $2.6 < \delta t \lesssim 6$ days; and (3) $\gtrsim$50 candidates more promising than SN 2025ulz at $\delta t \gtrsim 6$ days (Figure 12). After further inspection, we find that none of these potential transients appear to be an unambiguous electromagnetic counterpart associated with S250818k—although some simply do not have enough *publicly available* photometry to draw any conclusions. In the future, a coordinated follow-up observation strategy that continues to observe all promising candidates will help shield our KNe searches against impostor SNe IIb.

With this in mind, we are building a publicly accessible website to automatically vet candidate counterparts to poorly localized events (e.g., GWs, neutrinos, poorly localized GRBs, etc.) using the quantitative scoring methodology introduced in this work. This Tool for Rapid Object Vetting and Examination (TROVE) (https://astro-trove.github.io/), will include both a web application and application programming interface for scoring possible counterparts to poorly localized events. TROVE is under active development and will be made publicly available in the next $\sim$year. In the future, the TROVE candidate vetting will assist with community coordination of follow-up of poorly localized events, working to prevent future contaminating transients from dominating the KN search.

Acknowledgments

Time-domain research by the University of Arizona team and D.J.S. is supported by National Science Foundation (NSF) grants 2108032, 2308181, 2407566, and 2432036 and the Heising-Simons Foundation under grant #2020-1864. N.F. acknowledges support from the National Science Foundation Graduate Research Fellowship Program under grant No. DGE-2137419. C.D.K. gratefully acknowledges support from the NSF through AST-2432037, the HST Guest Observer Program through HST-SNAP-17070 and HST-GO-17706, and from JWST Archival Research through JWST-AR-6241 and JWST-AR-5441. K.D.A. and C.T.C. acknowledge support provided by the NSF through award AST-2307668. K.D.A. gratefully acknowledges support from the Alfred P. Sloan Foundation. J. R. was supported by NASA through the NASA Hubble Fellowship grant #HST-HF2-51587.001-A awarded by the Space Telescope Science Institute, which is operated by the

Association of Universities for Research in Astronomy, Inc., for NASA, under contract NAS5-26555. K.A.B. is supported by an LSST-DA Catalyst Fellowship; this publication was thus made possible through the support of grant 62192 from the John Templeton Foundation to LSST-DA. The Berger Time-Domain group at Harvard is supported by NSF and NASA, including AST-2206110.

The work of J.E.A. is supported by NOIRLab, which is managed by the Association of Universities for Research in Astronomy (AURA) under a cooperative agreement with the U.S. National Science Foundation. D.L.C. acknowledges support from the Science and Technology Facilities Council (STFC) grant number ST/X001121/1. K.J.D. acknowledges support from NSF grant PHY-2308986 and the Heising-Simons Foundation grant # 2022-3927. She also respectfully acknowledges that the University of Arizona is home to the O'odham and the Yaqui. She respects and honors the ancestral caretakers of the land, from time immemorial until now, and into the future. This work is supported by the National Science Foundation under Cooperative Agreement PHY-2019786 (The NSF AI Institute for Artificial Intelligence and Fundamental Interactions, http://iaifi.org/). D.H. is supported by NASA grant HST-GO-17770.002-A. R.M. acknowledges support by the National Science Foundation under award No. AST-2224255. V.P. is in part supported by NASA grant 80NSSC24K0771 and NSF grant PHY-2145421 to the University of Arizona. M.R. acknowledges support from NASA (ATP: 80NSSC24K0932). N.V. acknowledges funding from the National Sciences and Engineering Research Council of Canada (NSERC) Postdoctoral Fellowship 599555.

Some observations reported here were obtained at the MMT Observatory, a joint facility of the University of Arizona and the Smithsonian Institution. We thank the Harvard and Northwestern teams for coordinating a joint MMT/Binospec observation with the University of Arizona.

Some of the data presented herein were obtained at Keck Observatory, which is a private 501(c)3 nonprofit organization operated as a scientific partnership among the California Institute of Technology, the University of California, and the National Aeronautics and Space Administration. The Observatory was made possible by the generous financial support of the W. M. Keck Foundation. The authors wish to recognize and acknowledge the very significant cultural role and reverence that the summit of Maunakea has always had within the Native Hawaiian community. We are most fortunate to have the opportunity to conduct observations from this mountain.

This research is based on observations made with the NASA/ESA Hubble Space Telescope obtained from the Space Telescope Science Institute, which is operated by the Association of Universities for Research in Astronomy, Inc., under NASA contract NAS5–26555. These observations are associated with program(s) GO-17450 and GO-17805 (PI: Troja). The specific observations analyzed can be accessed via MAST: doi:10.17909/echw-bs67.

The National Radio Astronomy Observatory (NRAO) is a facility of the National Science Foundation operated under cooperative agreement by Associated Universities, Inc. GMRT observations were obtained for this study. We thank the staff of the GMRT who have made these observations possible. This work is based on observations carried out under project number S25CS with the IRAM NOEMA Interferometer. IRAM is supported by INSU/CNRS (France), MPG (Germany), and IGN (Spain). The Submillimeter Array is a joint project between the Smithsonian Astrophysical Observatory and the Academia Sinica Institute of Astronomy and Astrophysics and is funded by the Smithsonian Institution and the Academia Sinica. We recognize that Maunakea is a culturally important site for the indigenous Hawaiian people; we are privileged to study the cosmos from its summit.

Facilities: HST, Keck:I (LRIS), MMT (Binospec), S-PLUS, GMRT, MeerKAT, VLA, NOEMA, SMA.

Software: Astropy (Astropy Collaboration et al. 2013, 2018, 2022), `astropy-healpix` (Astropy Collaboration et al. 2022), Astroquery (A. Ginsburg et al. 2019), Astro-SCRAPPY (C. McCully et al. 2018), Beautiful Soup (L. Richardson 2023), Binospec IDL Pipeline (J. Kansky et al. 2019), CASA (J. P. McMullin et al. 2007; Team CASA et al. 2022), `crispy-bootstrap4` (D. Smith 2022), `dateutil` (G. Niemeyer et al. 2021), Django (Django Software Foundation 2023), `django-bootstrap4` (D. Verheul 2021), `django-crispy-forms` (M. Araujo 2023), Django Extensions (M. Trier & B. van Oostveen 2023), Django Filter (C. Gibson 2021), `django-gravatar` (T. Waddington 2020), `django-guardian` (L. Balcerzak 2021), Django REST Framework (T. Christie 2022), `django-webpack-loader` (O. Lone 2022), `dustmaps`G. Green (2018), `fastavro` (M. Tebeka 2022), Flask (Pallets Projects. 2022), Flask-SQLAlchemy (Pallets Projects. 2021), `fundamentals` (D. Young 2023), `gracedb-sdk` (L. Singer 2022), HEALPix Alchemy (L. P. Singer et al. 2022), `healpy` (A. Zonca et al. 2019), Hop Client (P. Godwin 2022), Hopskotch (SCiMMA Project 2023), IRAF (D. Tody 1986, 1993), Light Curve Fitting (G. Hosseinzadeh & S. Gomez 2022), `ligo.skymap` (L. P. Singer & L. R. Price 2016), `lmfit` (M. Newville et al. 2023), Apache Kafka (Apache Software Foundation. 2023), Matplotlib (J. D. Hunter 2007), MOCPy (M. Baumann et al. 2023), NumPy (C. R. Harris et al. 2020), Paramiko (J. Forcier 2023), Photutils (L. Bradley et al. 2022), Pillow (A. Murray et al. 2023), `plotly.py` (Plotly 2023), PostgreSQL (PostgreSQL Global Development Group 2022), Psycopg (F. Di Gregorio & D. Varrazzo 2023), Python-Markdown (M. Stienstra et al. 2023), Q3C (S. Koposov & O. Bartunov 2006), Requests (K. Reitz 2023), SAGUARO TOM (G. Hosseinzadeh et al. 2023), SASSy Q3C Models (P. N. Daly et al. 2023), SciPy (P. Virtanen et al. 2020), `setuptools` (Python Packaging Authority 2023), `sip_tpv` (D. L. Shupe et al. 2012), Source Extractor (E. Bertin & S. Arnouts 1996, 2010), `specutils` (N. Earl et al. 2023), SQLAlchemy (M. Bayer 2012), SWarp (E. Bertin 2010), TOM Toolkit (D. Collom et al. 2020; W. Lindstrom et al. 2022), `tom-alertstreams` (TOM Toolkit Project & W. Lindstrom 2023), `tom_nonlocalizedevents` (TOM Toolkit Project et al. 2023), `urllib3` (A. Petrov et al. 2023), `voevent-parse` (T. D. Staley 2014), Watchdog (Y. Mangalapilly 2023).

Appendix A
Detailed Method for Deriving the Distance Score

We begin with the following parameters:

1. $\overline{D_{\rm GW}}\rightarrow$ The mean distance to the GW event at the position of the candidate as given by the IGWN alerts.

2. $\sigma_{\rm GW} \rightarrow$ The symmetric uncertainty on $\overline{D_{\rm GW}}$ reported in the IGWN alert.
3. $\overline{D_{\rm C}} \rightarrow$ The mean derived luminosity distance to the host galaxy with the lowest $P_{\rm cc}$ score.
4. $\sigma_{\rm C}^{+}$ and $\sigma_{\rm C}^{-} \rightarrow$ The positive and negative uncertainties on $\overline{D_{\rm C}}$, respectively. In the case of a $\overline{D_{\rm C}}$ derived from a spectroscopic redshift or a photometric redshift with symmetric uncertainties $\sigma_{\rm C} = \sigma_{\rm C}^{+} = \sigma_{\rm C}^{-}$.

For the GW event, the uncertainties are symmetric, so, assuming the uncertainties are Gaussian, the probability distribution of the distance to the GW event is given by Equation (A1)

$$\mathrm{P_{GW}}(D) = \frac{1}{\sigma_{\rm GW}\sqrt{2\pi}} \exp\left[-\frac{1}{2}\left(\frac{D-\overline{D_{\rm GW}}}{\sigma_{\rm GW}}\right)^2\right]. \quad \text{(A1)}$$

Since the uncertainty on the distance to the candidate event is potentially asymmetric, we use a split normal distribution (Equation A2) to describe the probability distribution.

$$\mathrm{P_C}(D) = \sqrt{\frac{2}{\pi(\sigma_{\rm C}^{+}+\sigma_{\rm C}^{-})^2}} \times \begin{cases} \exp\left[-\frac{1}{2}\left(\frac{D-\overline{D_{\rm C}}}{\sigma_{\rm C}^{+}}\right)^2\right], & D > \overline{D_{\rm C}} \\ \exp\left[-\frac{1}{2}\left(\frac{D-\overline{D_{\rm C}}}{\sigma_{\rm C}^{-}}\right)^2\right], & D \leqslant \overline{D_{\rm C}} \end{cases}. \quad \text{(A2)}$$

The normalization factor $2/[\sqrt{\pi}(\sigma_{\rm C}^{+}+\sigma_{\rm C}^{-})]$ is derived by integrating the piecewise function from $-\infty \rightarrow \infty$. From these two probability distributions, we compute the Bhattacharyya coefficient (A. Bhattacharyya 1943)—a nonparametric, normalized measure of the distances between the distributions such that 0 indicates no similarity and 1 indicates identical distributions

$$\mathrm{S_{dist}} = \int_0^{\infty} \sqrt{\mathrm{P_{GW}}(D) \times P_{\rm C}(D)} \quad dD \quad \text{(A3)}$$

$$= \left[\pi\sigma_{\rm GW}(\sigma_{\rm C}^{+}+\sigma_{\rm C}^{-})\right]^{-1/2} \int_0^{\infty} \times \left[\exp\left[-\frac{1}{2}\left(\frac{D-\overline{D_{\rm GW}}}{\sigma_{\rm GW}}\right)^2\right] \times \begin{cases} \exp\left[-\frac{1}{2}\left(\frac{D-\overline{D_{\rm C}}}{\sigma_{\rm C}^{+}}\right)^2\right], & D > \overline{D_{\rm C}} \\ \exp\left[-\frac{1}{2}\left(\frac{D-\overline{D_{\rm C}}}{\sigma_{\rm C}^{-}}\right)^2\right], & D \leqslant \overline{D_{\rm C}} \end{cases}\right]^{1/2} \mathrm{dD} \quad \text{(A4)}$$

where $S_{\rm dist}$ is the score we assign for the distance association step in our vetting algorithm. In practice, to derive a score for the distance association, we integrate Equation (A4) numerically using `numpy.trapezoid` over a range $0 \rightarrow 10{,}000$ Mpc.

Appendix B
Candidates Table

All of the candidates are ranked by their score in Table 3.

Table 3
Candidate Scores

TNS Name	R.A.	Decl.	Overall Score	Two-dimensional Score	Point Source Score	Distance Score	Peak Luminosity (erg/s)	Time of Peak (days)	Decay Rate (mag/day)	Predetection Score
AT2025usl	237.1445	32.2938	0.73	0.85	1.00	0.86	7.42×10^{41}	⋯	⋯	1
AT2025uuf	310.1678	64.6115	0.51	0.59	1.00	0.87	5.11×10^{41}	⋯	⋯	1
AT2025uus	244.2946	39.6485	0.41	0.97	1.00	0.42	9.88×10^{41}	⋯	⋯	1
AT2025uua	261.4404	51.9287	0.39	0.39	1.00	1.00	8.90×10^{41}	⋯	⋯	1
AT2025uow	53.3796	−30.0963	0.38	0.45	1.00	0.87	2.38×10^{42}	0.05	0.13	1
AT2025usk	241.2050	35.7908	0.35	0.99	1.00	0.35	1.04×10^{42}	⋯	⋯	1
AT2025uvu	236.7145	29.9994	0.31	0.76	1.00	0.42	5.68×10^{41}	⋯	⋯	1
AT2025wfs	236.5714	31.8389	0.30	0.83	1.00	0.36	3.44×10^{41}	⋯	⋯	1
AT2025uxu	270.6914	56.4917	0.24	0.30	1.00	0.80	4.97×10^{41}	0.16	0.25	1
AT2025uut	283.5697	60.0326	0.15	0.52	1.00	0.29	6.85×10^{41}	⋯	⋯	1
AT2025utu	301.9844	61.3465	0.15	0.25	1.00	0.63	6.34×10^{41}	0.37	0.33	1
AT2025usn	237.6131	30.3337	0.12	0.64	1.00	0.20	1.04×10^{42}	⋯	⋯	1
AT2025uuc	264.9940	53.3377	0.10	0.35	1.00	0.30	8.79×10^{41}	⋯	⋯	1
AT2025uog	58.3270	−33.1844	0.09	0.52	1.00	0.18	1.60×10^{42}	0.05	0.20	1
AT2025uul	237.0139	29.7992	0.09	0.64	1.00	0.15	7.60×10^{41}	⋯	⋯	1
AT2025uur	236.7506	30.5273	0.09	0.81	1.00	0.12	6.46×10^{41}	⋯	⋯	1
AT2025uzu	244.2891	41.7935	0.09	0.53	1.00	0.17	7.50×10^{41}	0.14	0.12	1
AT2025unm	247.0348	42.0573	0.08	0.91	1.00	0.95	4.94×10^{41}	0.12	0.02	1
AT2025uuk	262.3959	54.6045	0.08	0.30	1.00	0.28	1.30×10^{42}	⋯	⋯	1
AT2025war	298.4335	60.7029	0.07	0.19	1.00	0.41	5.77×10^{41}	⋯	⋯	1
AT2025uvt	238.8852	31.0098	0.07	0.59	1.00	0.12	3.08×10^{41}	⋯	⋯	1
AT2025wek	237.0823	32.7603	0.07	0.83	1.00	0.09	8.83×10^{41}	⋯	⋯	1
AT2025uug	285.5158	59.3271	0.07	0.44	1.00	0.17	6.74×10^{41}	⋯	⋯	1
AT2025uub	300.2631	61.9816	0.06	0.49	1.00	0.13	1.80×10^{42}	0.37	0.13	1
AT2025uya	248.6400	43.9504	0.04	0.86	1.00	0.05	8.30×10^{41}	⋯	⋯	1
AT2025uuu	267.1103	56.0134	0.04	0.28	1.00	0.16	4.60×10^{41}	⋯	⋯	1
AT2025vag	232.3371	24.4240	0.03	0.57	1.00	0.07	3.89×10^{41}	0.18	0.13	1
AT2025vaj	245.1994	42.0982	0.03	0.81	1.00	0.04	1.06×10^{42}	0.12	0.12	1
AT2025unj	242.1796	40.0271	0.03	0.49	1.00	0.71	5.36×10^{41}	0.18	−1.48	1
AT2025urh	259.7336	50.9121	0.02	0.42	1.00	0.05	4.13×10^{41}	0.20	0.20	1
AT2025uvs	269.2303	55.3516	0.02	0.33	1.00	0.07	9.93×10^{41}	1.30	2.24	1
AT2025utq	262.9452	54.7965	0.02	0.29	1.00	0.94	1.74×10^{42}	2.30	0.44	0.10
AT2025uuq	244.6472	37.9425	0.02	0.71	1.00	0.04	1.75×10^{42}	⋯	⋯	1
AT2025usm	236.9292	30.5482	0.02	0.80	1.00	0.03	4.90×10^{41}	⋯	⋯	1
AT2025unp	241.0241	35.6278	0.02	0.99	1.00	0.30	9.40×10^{41}	1.12	−0.01	1
AT2025uzf	255.1251	49.6713	0.01	0.41	1.00	0.45	4.84×10^{41}	0.20	0.02	1
AT2025vtz	215.8520	−1.2628	0.01	0.05	1.00	0.36	2.84×10^{41}	⋯	⋯	1
AT2025van	247.9201	40.5134	0.01	0.43	1.00	0.03	6.46×10^{41}	⋯	⋯	1
AT2025uph	297.0605	64.6750	0.01	0.48	1.00	0.40	1.81×10^{42}	0.37	0.06	1
AT2025uzl	241.6009	37.7818	0.01	0.95	1.00	0.18	8.20×10^{41}	0.12	0.08	1
AT2025uzq	232.9914	25.2775	0.01	0.58	1.00	0.20	7.41×10^{41}	0.14	0.00	1
AT2025vau	234.3892	29.6586	0.00	0.50	0.00	⋯	⋯	⋯	⋯	1
AT2025utv	258.7515	51.3671	0.00	0.50	1.00	0.34	2.23×10^{42}	19.22	−0.03	1
AT2025vam	235.0854	30.5155	0.00	0.68	1.00	0.27	2.05×10^{42}	11.23	−0.86	1
AT2025uzx	242.0438	38.3653	0.00	0.92	0.00	⋯	⋯	⋯	⋯	1
AT2025unn	239.1654	33.2560	0.00	0.92	1.00	0.09	7.43×10^{41}	0.12	0.09	1
AT2025vaf	244.7487	38.1098	0.00	0.70	1.00	0.03	4.40×10^{41}	1.11	−0.09	1
AT2025uzk	239.9571	33.5515	0.00	0.82	1.00	0.23	1.80×10^{42}	11.22	−0.54	1
SN 2025uuw	249.2317	44.3800	0.00	0.84	1.00	0.87	9.53×10^{42}	20.21	−2.66	1
AT2025uzr	241.4425	37.0061	0.00	0.99	1.00	0.49	1.95×10^{42}	17.22	−0.32	1
AT2025uzh	239.1768	34.1537	0.00	0.97	0.00	⋯	⋯	⋯	⋯	1
AT2025val	245.4769	40.0921	0.00	0.96	1.00	0.00	7.44×10^{41}	4.13	−0.36	1
AT2025vab	241.8167	36.9921	0.00	1.00	1.00	0.00	8.11×10^{41}	⋯	⋯	1
AT2025vas	242.6047	36.9211	0.00	0.95	1.00	0.00	4.43×10^{41}	0.17	−1.51	1
AT2025unk	246.3895	40.7304	0.00	0.89	1.00	0.00	8.41×10^{41}	0.14	0.30	1
AT2025uzw	241.2052	35.2971	0.00	0.88	1.00	0.00	5.17×10^{41}	1.12	−0.17	1
AT2025uzy	231.0306	23.8806	0.00	0.55	0.00	⋯	⋯	⋯	⋯	1
AT2025vat	233.0136	27.5937	0.00	0.42	1.00	0.41	6.80×10^{41}	4.14	−0.01	1
AT2025vad	237.2357	28.6869	0.00	0.43	1.00	0.01	5.86×10^{41}	1.13	−0.13	1
AT2025uup	297.7439	61.5513	0.00	0.44	1.00	0.06	4.63×10^{41}	9.33	−0.01	1
AT2025uxs	236.0598	27.4783	0.00	0.44	1.00	0.96	8.88×10^{42}	20.19	−2.67	1
AT2025unh	260.4936	52.5422	0.00	0.44	1.00	0.19	2.41×10^{42}	19.23	−0.56	0.10

Table 3
(Continued)

TNS Name	R.A.	Decl.	Overall Score	Two-dimensional Score	Point Source Score	Distance Score	Peak Luminosity (erg/s)	Time of Peak (days)	Decay Rate (mag/day)	Predetection Score
AT2025uuv	311.7227	65.1269	0.00	0.46	1.00	0.12	6.56×10^{41}	2.38	−0.13	1
AT2025uzd	251.2641	44.2983	0.00	0.46	1.00	0.96	4.14×10^{42}	19.21	−0.90	1
AT2025ung	251.2002	44.2290	0.00	0.46	0.00	…	…	…	…	1
AT2025uuh	283.6991	60.2078	0.00	0.49	0.00	…	…	…	…	1
AT2025utw	296.9660	64.5091	0.00	0.48	1.00	0.63	7.50×10^{41}	9.33	−0.37	1
AT2025uzv	232.9374	25.0276	0.00	0.54	1.00	0.16	4.92×10^{41}	4.14	−0.34	1
AT2025unl	250.1465	46.7436	0.00	0.52	1.00	0.19	5.63×10^{41}	0.19	−0.27	1
AT2025utz	247.7828	40.7123	0.00	0.51	1.00	0.00	1.30×10^{42}	…	…	1
AT2025vaa	254.1146	46.8251	0.00	0.50	1.00	0.00	3.61×10^{41}	0.20	0.03	1
AT2025uzz	238.4062	36.1216	0.00	0.39	0.00	…	…	…	…	1
AT2025uzo	234.0232	25.5990	0.00	0.34	1.00	0.10	1.07×10^{42}	4.14	−0.34	1
AT2025utr	271.9448	56.8702	0.00	0.32	1.00	0.83	2.44×10^{42}	19.25	−0.27	1
AT2025uzg	233.7461	24.8628	0.00	0.32	1.00	0.21	5.61×10^{41}	4.14	−0.40	1
AT2025uqe	257.9832	49.1794	0.00	0.33	1.00	0.83	1.83×10^{42}	15.26	−0.87	1
AT2025uxo	248.8884	41.0161	0.00	0.33	1.00	0.33	4.10×10^{42}	16.24	−1.76	1
AT2025usy	268.8021	56.0339	0.00	0.29	1.00	0.75	1.53×10^{42}	19.24	−1.04	1
AT2025utt	267.5892	54.9656	0.00	0.28	1.00	0.05	1.75×10^{42}	19.24	−0.26	1
AT2025uzi	244.8820	36.8049	0.00	0.28	1.00	0.26	5.88×10^{41}	4.10	−0.04	1
AT2025vae	234.2500	24.4686	0.00	0.29	1.00	0.15	7.48×10^{41}	1.13	−0.39	1
AT2025vao	257.7600	48.7028	0.00	0.27	1.00	0.02	5.70×10^{41}	1.23	−0.26	1
AT2025uno	231.2551	26.2796	0.00	0.27	1.00	0.00	5.86×10^{41}	0.14	0.14	1
AT2025vfa	246.2516	45.0537	0.00	0.26	1.00	0.11	9.01×10^{42}	20.21	−3.12	1
AT2025uui	239.7301	30.9933	0.00	0.26	1.00	0.17	1.69×10^{42}	11.23	−0.87	1
AT2025uuo	257.8897	51.5603	0.00	0.35	1.00	0.02	1.63×10^{42}	…	…	1
AT2025uud	313.4742	65.1826	0.00	0.39	0.00	…	…	…	…	1
AT2025uzn	235.2292	31.3958	0.00	0.41	0.00	…	…	…	…	1
SN 2025vnt	237.5921	29.0246	0.00	0.42	1.00	0.98	6.51×10^{42}	20.19	−3.44	1
AT2025vie	273.2270	58.9476	0.00	0.24	0.00	…	…	…	…	1
AT2025vay	230.7166	24.8829	0.00	0.25	1.00	0.07	9.08×10^{41}	4.09	−0.13	1
AT2025vav	235.3140	32.6537	0.00	0.25	1.00	0.01	4.18×10^{41}	4.14	−0.08	1
AT2025var	232.6559	28.8539	0.00	0.25	1.00	0.19	6.01×10^{41}	0.14	0.06	1
AT2025uzs	240.9930	32.4010	0.00	0.20	1.00	0.06	4.81×10^{41}	0.18	−4.74	1
AT2025vpk	43.2178	−11.1210	0.00	0.24	1.00	0.52	3.82×10^{42}	20.12	−0.71	1
AT2025uzj	233.5968	23.1899	0.00	0.21	1.00	0.02	7.71×10^{41}	4.09	−0.13	1
AT2025uql	267.2360	57.8759	0.00	0.22	1.00	0.28	2.43×10^{42}	19.25	−0.02	1
AT2025uzm	234.2632	31.8666	0.00	0.19	1.00	0.21	7.87×10^{41}	4.14	−0.13	1
AT2025uty	265.4641	52.4306	0.00	0.18	1.00	0.00	8.40×10^{41}	…	…	1
AT2025utx	251.0454	42.4653	0.00	0.16	0.00	…	…	…	…	1
AT2025uor	58.3948	−31.3176	0.00	0.15	0.00	…	…	…	…	1
AT2025vac	239.7555	40.2066	0.00	0.14	1.00	0.02	4.14×10^{41}	4.13	−0.08	1
AT2025vax	241.0788	32.3593	0.00	0.20	1.00	0.23	9.97×10^{41}	0.23	−0.78	1
AT2025whj	258.5650	53.6545	0.00	0.20	1.00	0.49	1.69×10^{42}	11.17	−1.93	1
AT2025vqh	270.4048	59.0380	0.00	0.20	1.00	0.18	2.30×10^{42}	19.25	−0.95	1
AT2025usb	53.2648	−31.3207	0.00	0.13	0.00	…	…	…	…	1
AT2025uzp	229.7613	25.6649	0.00	0.13	0.00	…	…	…	…	1
AT2025vap	265.4473	52.2285	0.00	0.14	1.00	0.09	1.39×10^{42}	7.30	−0.34	1
AT2025upw	222.0841	9.1170	0.00	0.12	1.00	0.91	5.99×10^{42}	15.95	−0.46	1
AT2025uzt	236.2462	35.7672	0.00	0.09	1.00	0.03	4.93×10^{41}	0.19	−1.53	1
AT2025wju	42.7855	−14.6134	0.00	0.12	1.00	0.91	2.96×10^{42}	19.34	−2.12	1
AT2025usa	286.0330	63.8107	0.00	0.12	1.00	0.07	1.02×10^{42}	1.30	0.28	1
AT2025uzc	235.9834	25.1267	0.00	0.10	0.00	…	…	…	…	1
AT2025vah	239.4820	29.2197	0.00	0.08	1.00	0.06	7.62×10^{41}	1.13	−0.13	1
AT2025vak	237.6184	38.5752	0.00	0.08	0.00	…	…	…	…	1
AT2025uze	306.3231	67.3743	0.00	0.09	1.00	0.16	1.54×10^{42}	13.32	−0.43	1
AT2025uxm	239.2477	29.4235	0.00	0.08	0.00	…	…	…	…	1
AT2025uso	244.2393	35.0558	0.00	0.05	1.00	0.88	9.78×10^{42}	20.21	−2.55	1
AT2025unr	220.8751	13.1996	0.00	0.06	1.00	0.62	1.75×10^{42}	8.22	−0.90	1
AT2025vai	242.0910	32.7409	0.00	0.07	0.00	…	…	…	…	1
SN 2025ulz	237.9758	30.9024	0.00	0.66	1.00	0.68	2.12×10^{42}	26.76	−3.07	1

(This table is available in its entirety in machine-readable form in the online article.)

Appendix C
Photometry Tables

The optical and ultraviolet photometry is given in Table 4 and the radio photometry is given in Table 5.

Table 4
SN 2025ulz Ultraviolet, Optical, and Infrared Photometry

MJD	Filter	Magnitude	Magnitude Error	Telescope (Source)
60901.64	*u*	>22.10	⋯	WFST (Z. Y. Liu et al. 2025)
60901.67	*g*	>22.40	⋯	WFST (Z. Y. Liu et al. 2025)
60903.32	*o*	>21.48	⋯	ATLAS (This work)
60903.32	*o*	>21.23	⋯	ATLAS (This work)
60903.32	*o*	21.61	0.35	ATLAS (This work)
60904.22	*r*	>21.01	⋯	P48 (TNS)
60904.23	*y*	>19.70	⋯	PS (M. Nicholl et al. 2025)
60905.19	*g*	20.99	0.13	P48 (TNS)
60905.24	*r*	21.29	0.13	P48 (TNS)
60905.82	*r*	21.43	0.06	Wendelstein (M. Busmann et al. 2025)
60905.82	*g*	21.25	0.03	Wendelstein (M. Busmann et al. 2025)
60906.13	*J*	>19.30	⋯	WINTER (G. Mo et al. 2025)
60906.84	*r*	21.83	0.06	Wendelstein (X. J. Hall et al. 2025)
60906.84	*g*	22.08	0.09	Wendelstein (X. J. Hall et al. 2025)
60907.23	*r*	22.60	0.00	Gemini (B. O'Connor et al. 2025)
60907.23	*g*	23.00	0.00	Gemini (B. O'Connor et al. 2025)
60907.30	*g*	22.90	0.40	PS (J. H. Gillanders et al. 2025)
60907.31	*r*	22.20	0.20	PS (J. H. Gillanders et al. 2025)
60907.31	*r*	22.05	0.20	PS1 (TNS)
60907.33	*I*	21.80	0.20	PS (J. H. Gillanders et al. 2025)
60907.34	*z*	21.40	0.20	PS (J. H. Gillanders et al. 2025)
60907.60	*g*	22.71	0.10	WFST (Z. Y. Liu et al. 2025)
60907.61	*r*	22.78	0.16	WFST (Z. Y. Liu et al. 2025)
60907.63	*r*	22.80	0.30	JinShan (J. An et al. 2025a)
60907.65	*u*	23.24	0.24	WFST (Z. Y. Liu et al. 2025)
60907.88	*r*	23.20	0.20	NOT (D. B. Malesani et al. 2025)
60908.28	*r*	22.85	0.15	CFH (S. Antier et al. 2025)
60908.90	*r*	23.40	⋯	GTC (R. L. Becerra et al. 2025b)
60908.91	*r*	>21.72	⋯	STEP/T80N (A. Santos et al. 2025)
60908.92	*i*	>21.62	⋯	STEP/T80N (A. Santos et al. 2025)
60909.14	*i*	23.10	0.25	COLIBRI (C. Angulo et al. 2025)
60909.20	*i*	>22.96	⋯	MMT (This work)
60909.21	*r*	>22.90	⋯	MMT (This work)
60909.26	*i*	22.40	0.30	PS (J. H. Gillanders et al. 2025)
60909.84	F336W	23.85	0.30	Hubble WFC3/UVIS (E. Troja et al. 2025, re-reduced in this work)
60909.94	F110W	22.87	0.23	Hubble WFC3/IR (E. Troja et al. 2025, re-reduced in this work)
60910.17	F160W	22.15	0.30	Hubble WFC3/IR (E. Troja et al. 2025, re-reduced in this work)
60910.26	*i*	22.50	0.30	PS (J. H. Gillanders et al. 2025)
60911.15	*i*	22.00	0.10	COLIBRI (C. Angulo et al. 2025)
60911.26	*i*	22.10	0.20	PS (J. H. Gillanders et al. 2025)
60912.26	*i*	21.60	0.10	PS (J. H. Gillanders et al. 2025)
60912.86	*r*	21.45	0.44	STEP (This work)
60912.88	*i*	21.37	0.28	STEP (This work)
60913.90	F606W	22.03	0.03	Hubble WFC3/UVIS (PI: Troja; This work)
60914.82	F110W	21.81	0.02	Hubble WFC3/IR (PI: Troja; This work)
60914.99	*r*	>21.04	⋯	SOAR (This work)
60915.00	*i*	21.04	0.28	SOAR (This work)
60915.01	*z*	>20.76	⋯	SOAR (This work)
60915.47	F160W	21.79	0.05	Hubble WFC3/IR (PI: Troja; This work)
60916.28	*o*	>20.43	⋯	ATLAS (This work)
60917.19	*z*	20.40	0.08	MMT (This work)
60917.22	*i*	20.28	0.09	MMT (This work)
60919.25	*o*	>17.85	⋯	ATLAS (This work)
60922.24	*o*	20.18	0.29	ATLAS (This work)
60923.26	*o*	>20.12	⋯	ATLAS (This work)
60924.26	*o*	>20.15	⋯	ATLAS (This work)
60924.82	*r*	20.64	0.23	STEP (This work)
60924.83	*i*	20.70	0.23	STEP (This work)
60925.26	*o*	>19.46	⋯	ATLAS (This work)
60929.67	*r*	20.82	0.11	HCT (V. Swain et al. 2025)
60931.81	*i*	20.41	0.18	T80 (This work)
60931.82	*r*	20.77	0.21	T80 (This work)

(This table is available in its entirety in machine-readable form in the online article.)

Table 5
Summary of Radio Observations for SN 2025ulz

Telescope	MJD	$\nu_{\rm eff}$ (GHz)	$\theta_{\rm B,major} \times \theta_{\rm B,minor}$	$\theta_{\rm PA}$	Flux Density (μJy)	Source
GMRT	60913.6	1.26	$2\farcs5 \times 2\farcs0$	-5°	<80	G. Bruni et al. (2025a), this work
MeerKAT	60932	0.82	$18\farcs3 \times 14\farcs7$	167°	185 ± 44	G. Bruni et al. (2025d), re-reduced in this work
MeerKAT	60932	1.28	$8\farcs5 \times 7\farcs5$	27°	186 ± 18	G. Bruni et al. (2025d), re-reduced in this work
MeerKAT	60908	3.06	$8\farcs0 \times 3\farcs7$	163°	59 ± 5	G. Bruni et al. (2025b), re-reduced in this work
MeerKAT	60915	3.06	$4\farcs5'' \times 3\farcs8$	5°	83 ± 6	G. Bruni et al. (2025c), L. Rhodes et al. (2025), re-reduced in this work
MeerKAT	60931	3.06	$4\farcs3 \times 3\farcs9$	7°	76 ± 9	G. Bruni et al. (2025d), re-reduced in this work
NOEMA	60909.9	92	$3\farcs8 \times 2\farcs7$	54°	<63	This work
SMA	60908.3	225.5	$3\farcs2 \times 3\farcs0$	89.1°	<750	This work
VLA	60917.9	3	$1\farcs7 \times 1\farcs5$	−81°	<28	This work
VLA	60917.9	6	$1\farcs0 \times 0\farcs8$	−85°	<20	This work
VLA	60909.2	6	$1\farcs0 \times 0\farcs9$	90°	<18	This work
VLA	60917.9	10	$0\farcs7 \times 0\farcs5$	−80°	<20	This work
VLA	60911	3	⋯	⋯	<40	R. Ricci et al. (2025d)
VLA	60911	6	⋯	⋯	<25	R. Ricci et al. (2025d)
VLA	60908	10	⋯	⋯	<30	R. Ricci et al. (2025b)

Note. The reported uncertainties are 1σ statistical errors. Nondetections are reported as 3σ upper limits.

(This table is available in its entirety in machine-readable form in the online article.)

ORCID iDs

Noah Franz https://orcid.org/0000-0003-4537-3575
Bhagya Subrayan https://orcid.org/0000-0001-8073-8731
Charles D. Kilpatrick https://orcid.org/0000-0002-5740-7747
Griffin Hosseinzadeh https://orcid.org/0000-0002-0832-2974
David J. Sand https://orcid.org/0000-0003-4102-380X
Kate D. Alexander https://orcid.org/0000-0002-8297-2473
Wen-fai Fong https://orcid.org/0000-0002-7374-935X
Collin T. Christy https://orcid.org/0000-0003-0528-202X
Jeniveve Pearson https://orcid.org/0000-0002-0744-0047
Tanmoy Laskar https://orcid.org/0000-0003-1792-2338
Brian Hsu https://orcid.org/0000-0002-9454-1742
Jillian Rastinejad https://orcid.org/0000-0002-9267-6213
Michael J. Lundquist https://orcid.org/0000-0001-9589-3793
Edo Berger https://orcid.org/0000-0002-9392-9681
K. Azalee Bostroem https://orcid.org/0000-0002-4924-444X
Clecio R. Bom https://orcid.org/0000-0003-4383-2969
Phelipe Darc https://orcid.org/0000-0001-8833-474X
Mark Gurwell https://orcid.org/0000-0003-0685-3621
Garrett K. Keating https://orcid.org/0000-0002-3490-146X
Phillip Noel https://orcid.org/0009-0006-0647-636X
Conor Ransome https://orcid.org/0000-0003-4175-4960
Luidhy Santana-Silva https://orcid.org/0000-0003-3402-6164
A. Souza Santos https://orcid.org/0000-0002-1420-3584
Manisha Shrestha https://orcid.org/0000-0002-4022-1874
Ramya Anche https://orcid.org/0000-0002-4989-6253
Jennifer E. Andrews https://orcid.org/0000-0003-0123-0062
Sanchayeeta Borthakur https://orcid.org/0000-0002-2724-8298
Nathaniel R. Butler https://orcid.org/0000-0002-9110-6673
Deanne L. Coppejans https://orcid.org/0000-0001-5126-6237
Kathryne J. Daniel https://orcid.org/0000-0003-2594-8052
Paul C. Duffell https://orcid.org/0000-0001-7626-9629
Tarraneh Eftekhari https://orcid.org/0000-0003-0307-9984
Carl E. Fields https://orcid.org/0000-0002-8925-057X
Alexander T. Gagliano https://orcid.org/0000-0003-4906-8447
Walter W. Golay https://orcid.org/0000-0001-7946-1034
Aldana Grichener https://orcid.org/0000-0002-2215-1841
Erika T. Hamden https://orcid.org/0000-0002-3131-7372
Daichi Hiramatsu https://orcid.org/0000-0002-1125-9187
Harsh Kumar https://orcid.org/0000-0003-0871-4641
Vikram Manikantan https://orcid.org/0000-0003-0547-6158
Raffaella Margutti https://orcid.org/0000-0003-4768-7586
Vasileios Paschalidis https://orcid.org/0000-0002-8099-9023
Kerry Paterson https://orcid.org/0000-0001-8340-3486
Daniel E. Reichart https://orcid.org/0000-0002-5060-3673
Mathieu Renzo https://orcid.org/0000-0002-6718-9472
Kali Salmas https://orcid.org/0009-0009-7182-6022
Genevieve Schroeder https://orcid.org/0000-0001-9915-8147
Nathan Smith https://orcid.org/0000-0001-5510-2424
Kristine Spekkens https://orcid.org/0000-0002-0956-7949
Jay Strader https://orcid.org/0000-0002-1468-9668
David E. Trilling https://orcid.org/0000-0003-4580-3790
Nicholas Vieira https://orcid.org/0000-0001-7815-7604
Benjamin Weiner https://orcid.org/0000-0001-6065-7483
Peter K. G. Williams https://orcid.org/0000-0003-3734-3587

References

A. J., N., Chandra, P., Krishna, A., & Anupama, G. C. 2022, ApJ, 934, 186
Ackley, K. 2025, arXiv:2510.15836
Ackley, K., Amati, L., Barbieri, C., et al. 2020, A&A, 643, A113
Ahumada, T., Anand, S., Bulla, M., et al. 2025, arXiv:2507.00357
Ahumada, T., Anand, S., Coughlin, M. W., et al. 2024, PASP, 136, 114201
Alam, S., Albareti, F. D., Allende Prieto, C., et al. 2015, ApJS, 219, 12
Alexander, K. D., Berger, E., Fong, W., et al. 2017, ApJL, 848, L21
Alexander, K. D., Margutti, R., Blanchard, P. K., et al. 2018, ApJL, 863, L18
Alexander, K. D., Schroeder, G., Paterson, K., et al. 2021, ApJ, 923, 66

An, F., Vaccari, M., Best, P. N., et al. 2024, MNRAS, 528, 5346
An, J., Liu, X., Zhu, Z. P., et al. 2025a, GCN, 41503, 1
An, J., Malesani, D. B., Xu, D., et al. 2025b, GCN, 40966, 1
Anand, S., Coughlin, M. W., Kasliwal, M. M., et al. 2021, NatAs, 5, 46
Anderson, G. E., Belkin, S., Leung, J. K., et al. 2024, GCN, 38189, 1
Andreoni, I., Goldstein, D. A., Anand, S., et al. 2019, ApJL, 881, L16
Andreoni, I., Goldstein, D. A., Kasliwal, M. M., et al. 2020, ApJ, 890, 131
Angulo, C., Watson, A. M., Dornic, D., et al. 2025, GCN, 41518, 1
Antier, S., Pillas, M., Akl, D., et al. 2025, GCN, 41519, 1
Antier, S., Agayeva, S., Aivazyan, V., et al. 2020a, MNRAS, 492, 3904
Antier, S., Agayeva, S., Almualla, M., et al. 2020b, MNRAS, 497, 5518
Apache Software Foundation., 2023 Apache Kafka, v3.5.1, https://kafka.apache.org/
Araujo, M., 2023 django–crispy-forms, v2.0-đ, GitHub, https://github.com/django-crispy-forms/django-crispy-forms
Arcavi, I., Gal-Yam, A., Yaron, O., et al. 2011, ApJL, 742, L18
Arcavi, I., Hosseinzadeh, G., Brown, P. J., et al. 2017a, ApJL, 837, L2
Arcavi, I., Hosseinzadeh, G., Howell, D. A., et al. 2017b, Natur, 551, 64
Armstrong, P., Tucker, B. E., Rest, A., et al. 2021, MNRAS, 507, 3125
Astropy Collaboration, Price-Whelan, A. M., Lim, P. L., et al. 2022, ApJ, 935, 167
Astropy Collaboration, Price-Whelan, A. M., Sipőcz, B. M., et al. 2018, AJ, 156, 123
Astropy Collaboration, Robitaille, T. P., Tollerud, E. J., et al. 2013, A&A, 558, A33
Balcerzak, L., 2021 django guardian, v2.4.0, GitHub, https://github.com/django-guardian/django-guardian
Banerjee, S., Botticella, M.-T., Brennan, S. J., et al. 2025, GCN, 41532, 1
Barna, T., Fremling, C., Ahumada, T., et al. 2025, PASP, 137, 084105
Barnes, J., & Kasen, D. 2013, ApJ, 775, 18
Baumann, M., Manon, Pineau, F.-X., et al. 2023, cds-astro/mocpy, v0.13.0, Zenodo, doi:10.5281/zenodo.8297730
Bayer, M. 2012, in The Architecture of Open Source Applications: Structure, Scale, and a Few More Fearless Hacks, ed. A. Brown & G. Wilson, 2 (aosabook.org) https://aosabook.org/en/v2/sqlalchemy.html
Becerra, R. L., Dichiara, S., Watson, A. M., et al. 2021, MNRAS, 507, 1401
Becerra, R. L., Troja, E., & Dichiara, S. 2025a, Second Epoch, GRB Coordinates Network, 41528, 1
Becerra, R. L., Watson, A. M., & Troja, E. 2025b, GCN, 41502, 1
Becerra, R. L., Yang, Y., Watson, A. M., Troja, E., & Lee, W. H. 2025c, GCN, 41544, 1
Beck, R., Szapudi, I., Flewelling, H., et al. 2021, MNRAS, 500, 1633
Becker, A., 2015 HOTPANTS: High Order Transform of PSF ANd Template Subtraction, Astrophysics Source Code Library, ascl:1504.004
Belczynski, K., Ryu, T., Perna, R., et al. 2017, MNRAS, 471, 4702
Benson, P. J., Herbst, W., Salzer, J. J., et al. 1994, AJ, 107, 1453
Berger, E., Price, P. A., Cenko, S. B., et al. 2005, Natur, 438, 988
Bersten, M. C., Benvenuto, O. G., Nomoto, K., et al. 2012, ApJ, 757, 31
Bertin, E., 2010 Resampling and Co-adding FITS Images Together-đ Astrophysics Source Code Library, record ascl:1010.068
Bertin, E., & Arnouts, S. 1996, A&AS, 117, 393
Bertin, E., & Arnouts, S., 2010 SExtractor: Source Extractor-đ Astrophysics Source Code Library, ascl:1010.064
Bhakta, D., Mooley, K. P., Corsi, A., et al. 2021, ApJ, 911, 77
Bhattacharyya, A. 1943, Sankhyā: The Indian Journal of Statistics (1933-1960), 6, 399, http://www.jstor.org/stable/25047806
Bloom, J. S., Kulkarni, S. R., & Djorgovski, S. G. 2002, AJ, 123, 1111
Bradley, L., Sipőcz, B., Robitaille, T., et al. 2022, Astropy/Photutils, v1.5.0, Zenodo, doi:10.5281/zenodo.6825092
Broderick, J. W., Shimwell, T. W., Gourdji, K., et al. 2020, MNRAS, 494, 5110
Bruni, G., Chandra, P., Christy, C. S. C., et al. 2025a, GCN, 41577, 1
Bruni, G., Piro, L., Gianfagna, G., & Thakur, A. L. 2025b, GCN, 41500, 1
Bruni, G., Piro, L., Gianfagna, G., & Thakur, A. L. 2025c, GCN, 41594, 1
Bruni, G., Piro, L., Gianfagna, G., & Thakur, A. L. 2025d, GCN, 42032, 1
Busmann, M., Hall, X. J., Gruen, D., O'Connor, B., & Palmese, A. 2025, GCN, 41421, 1
Team CASA, Bean, B., Bhatnagar, S., et al. 2022, PASP, 134, 114501
Chambers, K. C., Boer, T. D., Fairlamb, J., et al. 2025, Transient Name Server Discovery Report, 2025-3300, 1,
Chambers, K. C., Magnier, E. A., Metcalfe, N., et al. 2016, arXiv:1612.05560
Chang, S.-W., Onken, C. A., Wolf, C., et al. 2021, PASA, 38, e024
Chaudhary, S. S., Toivonen, A., Waratkar, G., et al. 2024, PNAS, 121, e2316474121
Chen, Y.-X., & Metzger, B. D. 2025, ApJ, 991, L22
Chevalier, R. A., & Soderberg, A. M. 2010, ApJL, 711, L40
CHIME/FRB Collaboration, Abbott, T. C., Amouyal, D., et al. 2025, ApJL, 989, L48
Christie, T., 2022 Django REST Framework, v3.14.0 GitHub, https://github.com/encode/django-rest-framework
Christy, C. T., Jayasinghe, T., Stanek, K. Z., et al. 2023, MNRAS, 519, 5271
Clemens, J. C., Crain, J. A., & Anderson, R. 2004, Proc. SPIE, 5492, 331
Collom, D., Lindstrom, L., Riba, A., et al. 2020, The TOM Toolkit, v2.0.0, Zenodo, doi:10.5281/zenodo.4437764
Coughlin, M. W., Tao, D., Chan, M. L., et al. 2018, MNRAS, 478, 692
Coughlin, M. W., Ahumada, T., Anand, S., et al. 2019, ApJL, 885, L19
Coughlin, M. W., Antier, S., Corre, D., et al. 2019, MNRAS, 489, 5775
Coulter, D. A., Foley, R. J., Kilpatrick, C. D., et al. 2017, Sci, 358, 1556
Cowperthwaite, P. S., Berger, E., Villar, V. A., et al. 2017, ApJL, 848, L17
Dahlen, D., Kwon, Y. G., Masiero, J. R., Spahr, T., & Mainzer, A. K. 2025, arXiv:2509.04666
Daly, P. N., Bostroem, K. A., & Hosseinzadeh, G. 2023, SASSy Q3C Models, v1.4.0, Zenodo, doi:10.5281/zenodo.8436176
Dálya, G., Galgóczi, G., Dobos, L., et al. 2018, MNRAS, 479, 2374
Darc, P., Bom, C., Kilpatrick, C., et al. 2025, PhRvD, 112, 063019
Das, K. K., Kasliwal, M. M., Fremling, C., et al. 2023, ApJ, 959, 12
de Jaeger, T., Shappee, B. J., Kochanek, C. S., et al. 2022, MNRAS, 509, 3427
de Wet, S., Groot, P. J., Bloemen, S., et al. 2021, A&A, 649, A72
DESI Collaboration, Adame, A. G., Aguilar, J., et al. 2024, AJ, 168, 58
Dichiara, S., Becerra, R. L., Chase, E. A., et al. 2021, ApJL, 923, L32
Di Gregorio, F., & Varrazzo, D., 2023 Psycopg, v2.9.6, GitHub, https://github.com/psycopg/psycopg2
Dimple, D., Gompertz, B. P., Levan, A. J., et al. 2025, MNRAS, 544, 548
Django Software Foundation, 2023 Django, v4.2, GitHub, https://github.com/django/django/
Dobie, D., Kaplan, D. L., Murphy, T., et al. 2018, ApJL, 858, L15
Dobie, D., Stewart, A., Murphy, T., et al. 2019, ApJL, 887, L13
Dobie, D., Stewart, A., Hotokezaka, K., et al. 2021, MNRAS, 510, 3794
Dolphin, A., 2016 DOLPHOT: Stellar photometry-đ Astrophysics Source Code Library, ascl:1608.013
Domínguez, A., Siana, B., Henry, A. L., et al. 2013, ApJ, 763, 145
Dong, Y., Eftekhari, T., Fong, W., et al. 2024, ApJ, 973, 133
Drout, M. R., Piro, A. L., Shappee, B. J., et al. 2017, Sci, 358, 1570
Earl, N., Tollerud, E., O'Steen, R., et al. 2023, astropy/specutils, v1.11.0, Zenodo, doi:10.5281/zenodo.804903
East, W. E., Paschalidis, V., & Pretorius, F. 2015, ApJ, 807, L3
Elmhamdi, A., Danziger, I. J., Branch, D., et al. 2006, A&A, 450, 305
Fabricant, D., Fata, R., Epps, H., et al. 2019, PASP, 131, 075004
Farah, J. R., Howell, D. A., Hiramatsu, D., et al. 2025a, arXiv:2509.12470
Farah, J. R., Howell, D. A., Terreran, G., et al. 2025b, ApJ, 984, 60
Flewelling, H. A., Magnier, E. A., Chambers, K. C., et al. 2020, ApJS, 251, 7
Fong, W., Berger, E., Blanchard, P. K., et al. 2017, ApJL, 848, L23
Fong, W., Berger, E., Margutti, R., & Zauderer, B. A. 2015, ApJ, 815, 102
Fong, W., Berger, E., Metzger, B. D., et al. 2014, ApJ, 780, 118
Fong, W., Gordon, A. C., Levan, A. J., et al. 2025, GCN, 41419, 1
Fong, W., Laskar, T., Rastinejad, J., et al. 2021, ApJ, 906, 127
Fong, W.-f., Nugent, A. E., Dong, Y., et al. 2022, ApJ, 940, 56
Forcier, J., 2023 Paramiko, 3.1.0, GitHub, https://github.com/paramiko/paramiko
Franz, N., Alexander, K. D., Gomez, S., et al. 2025, arXiv:2509.05405
Freeburn, J., O'Connor, B., Hall, X. J., et al. 2025, GCN, 41507, 1
Freedman, W. L., Madore, B. F., Hoyt, T., et al. 2020, ApJ, 891, 57
Frostig, D., Karambelkar, V. R., Stein, R. D., et al. 2025, PASP, 137, 074203
Gaia Collaboration, Vallenari, A., Brown, A. G. A., et al. 2023, A&A, 674, A1
Garcia, A., Morgan, R., Herner, K., et al. 2020, ApJ, 903, 75
Ghirlanda, G., Salafia, O. S., Paragi, Z., et al. 2019, Sci, 363, 968
Gibson, C., 2021 Django Filter, v21.1-đ, GitHub, https://github.com/carltongibson/django-filter
Gillanders, J. H., Huber, M. E., Chambers, K. C., et al. 2025, GCN, 41540, 1
Gillanders, J. H., Huber, M. E., Nicholl, M., et al. 2025, arXiv:2510.01142
Ginsburg, A., Sipőcz, B. M., Brasseur, C. E., et al. 2019, AJ, 157, 98
Godwin, P., 2022 Hop Client, v0.8.0, GitHub, https://github.com/scimma/hop-client
Goldstein, A., Veres, P., Burns, E., et al. 2017, ApJL, 848, L14
Goldstein, D. A., Andreoni, I., Nugent, P. E., et al. 2019, ApJL, 881, L7
Gomez, S., Hosseinzadeh, G., Cowperthwaite, P. S., et al. 2019, ApJL, 884, L55
Gompertz, B. P., Levan, A. J., & Tanvir, N. R. 2020, ApJ, 895, 58
Green, G. 2018, JOSS, 3, 695
Guillochon, J., Nicholl, M., Villar, V. A., et al. 2018, ApJS, 236, 6
Hajela, A., Margutti, R., Alexander, K. D., et al. 2019, ApJL, 886, L17

Hall, X. J., Busmann, M., Gruen, D., O'Connor, B., & Palmese, A. 2025, GCN, 41433, 1
Hallinan, G., Corsi, A., Mooley, K. P., et al. 2017, Sci, 358, 1579
Harris, C. R., Millman, K. J., van der Walt, S. J., et al. 2020, Natur, 585, 357
Hosseinzadeh, G., Bostroem, K. A., Ben-Ami, T., & Gomez, S. 2024, Light Curve Fitting, v0.10.0, Zenodo, doi:10.5281/zenodo.11405219
Hosseinzadeh, G., Cowperthwaite, P. S., Gomez, S., et al. 2019, ApJL, 880, L4
Hosseinzadeh, G., & Gomez, S. 2022, Light Curve Fitting, v0.7.0, Zenodo, doi:10.5281/zenodo.4312178
Hosseinzadeh, G., Paterson, K., Rastinejad, J. C., et al. 2024, ApJ, 964, 35
Hosseinzadeh, G., Rastinejad, J., & Shrestha, M. 2023, SAGUARO Target and Observation Manager, v1.0.0, Zenodo, doi:10.5281/zenodo.8436090
Hu, L., Cabrera, T., Palmese, A., et al. 2025, ApJ, 990, L46
Hunter, J. D. 2007, CSE, 9, 90
Jones, D. O., McGill, P., Manning, T. A., et al. 2024, arXiv:2410.17322
Kansky, J., Chilingarian, I., Fabricant, D., et al. 2019, PASP, 131, 075005
Karambelkar, V., Kasliwal, M. M., Hall, X. J. & tf Collaboration, & Growth Collaboration 2025, GCN, 41436, 1
Kasen, D., Fernández, R., & Metzger, B. D. 2015, MNRAS, 450, 1777
Kasen, D., Metzger, B., Barnes, J., Quataert, E., & Ramirez-Ruiz, E. 2017, Natur, 551, 80
Kasliwal, M. M., Anand, S., Ahumada, T., et al. 2020, ApJ, 905, 145
Kasliwal, M. M., Karambelkar, V., Fremling, C., et al. 2025, GCN, 41538, 1
Kasliwal, M. M., Nakar, E., Singer, L. P., et al. 2017, Sci, 358, 1559
Kennicutt, R. C., & Evans, N. J. 2012, ARA&A, 50, 531
Kennicutt, R. C., Jr. 1998, ARA&A, 36, 189
Kilpatrick, C. D. 2021, charliekilpatrick/hst123: hst123, v1.0.0, Zenodo, doi:10.5281/zenodo.5573941
Kilpatrick, C. D., Coulter, D. A., Arcavi, I., et al. 2021, ApJ, 923, 258
Kilpatrick, C. D., Drout, M. R., Auchettl, K., et al. 2021, MNRAS, 504, 2073
Kilpatrick, C. D., Foley, R. J., Kasen, D., et al. 2017, Sci, 358, 1583
Kim, S., Schulze, S., Resmi, L., et al. 2017, ApJL, 850, L21
Koposov, S., & Bartunov, O. 2006, ASPC, 351, 735, https://ui.adsabs.harvard.edu/abs/2006ASPC..351..735K
Kovlakas, K., Zezas, A., Andrews, J. J., et al. 2021, MNRAS, 506, 1896
Lamb, G. P., Tanvir, N. R., Levan, A. J., et al. 2019, ApJ, 883, 48
Laskar, T., Escorial, A. R., Schroeder, G., et al. 2022, ApJL, 935, L11
Levan, A. J., Fynbo, J. P. U., Hjorth, J., et al. 2009, GCN, 9958, 1, 1
Levan, A. J., Gompertz, B. P., Salafia, O. S., et al. 2024, Natur, 626, 737
Li, C., Zhang, Y., Cui, C., et al. 2024, AJ, 168, 233
Li, L.-X., & Paczynski, B. 1998, ApJ, 507, L59
Li, R. Z., Xu, X. P., Sun, H., et al. 2025, GCN, 41460, 1
LIGO Scientific Collaboration & Virgo Collaboration 2017, PhRvL, 119, 161101
LIGO Scientific Collaboration & Virgo Collaboration 2018, PhRvL, 121, 161101
LIGO Scientific Collaboration, Virgo Collaboration & KAGRA Collaboration. 2025a, GCN, 41437, 1
LIGO Scientific Collaboration, Virgo Collaboration & KAGRA Collaboration. 2025b, GCN, 41440, 1
LIGO Scientific Collaboration, Virgo Collaboration, et al. 2017a, ApJL, 848, L12
LIGO Scientific Collaboration, Virgo Collaboration, et al. 2017b, ApJL, 848, L13
Lindstrom, W., Chatelain, J., Collom, D., et al., 2022 TOM Toolkit: Target and Observation Manager Toolkit-đ Astrophysics Source Code, ascl:2208.004
Lipunov, V. M., Gorbovskoy, E., Kornilov, V. G., et al. 2017, ApJL, 850, L1
Liu, Z. Y., Xu, Z. L., Meng, D. Z., et al. 2025, GCN, 41461, 1
Lone, O., 2022 django-webpack-loader v1.6.0, GitHub, https://github.com/django-webpack/django-webpack-loader
Lundquist, M. J., Paterson, K., Fong, W., et al. 2019, ApJL, 881, L26
Makhathini, S., Mooley, K. P., Brightman, M., et al. 2021, ApJ, 922, 154
Malesani, D. B., Boye, A., Izzo, L., et al. 2025, GCN, 41492, 1
Mangalapilly, Y., 2023 Watchdog, v3.0.0, GitHub, https://github.com/gorakhargosh/watchdog
Margutti, R., Alexander, K. D., Xie, X., et al. 2018, ApJL, 856, L18
Margutti, R., Berger, E., Fong, W., et al. 2017, ApJL, 848, L20
Matheson, T., Filippenko, A. V., Ho, L. C., Barth, A. J., & Leonard, D. C. 2000, AJ, 120, 1499
Matthews, K., Neugebauer, G., Armus, L., & Soifer, B. T. 2002, AJ, 123, 753
McBrien, O. R., Smartt, S. J., Huber, M. E., et al. 2021, MNRAS, 500, 4213
McCully, C., Crawford, S., Kovacs, G., et al. 2018, astropy/astroscrappy v1.0.5, Zenodo, doi:10.5281/zenodo.1482019
McMullin, J. P., Waters, B., Schiebel, D., Young, W., & Golap, K. 2007, ASPC, 376, 127, https://ui.adsabs.harvard.edu/abs/2007ASPC..376..127M
Metzger, B. D. 2017, LRR, 20, 3
Metzger, B. D., Hui, L., & Cantiello, M. 2024, ApJ, 971, L34
Metzger, B. D., Martínez-Pinedo, G., Darbha, S., et al. 2010, MNRAS, 406, 2650
Milisavljevic, D., Margutti, R., Soderberg, A. M., et al. 2013, ApJ, 767, 71
Mo, G., Stein, R., Kasliwal, M., et al. 2025, GCN, 41456, 1
Mooley, K. P., Deller, A. T., Gottlieb, O., et al. 2018c, Natur, 561, 355
Mooley, K. P., Frail, D. A., Dobie, D., et al. 2018a, ApJL, 868, L11
Mooley, K. P., Nakar, E., Hotokezaka, K., et al. 2018b, Natur, 554, 207
Morales-Garoffolo, A., Elias-Rosa, N., Benetti, S., et al. 2014, MNRAS, 445, 1647
Morales-Garoffolo, A., Elias-Rosa, N., Bersten, M., et al. 2015, MNRAS, 454, 95
Morgan, R., Soares-Santos, M., Annis, J., et al. 2020, ApJ, 901, 83
Murguia-Berthier, A., Ramirez-Ruiz, E., Colle, F. D., et al. 2021, ApJ, 908, 152
Murphy, E. J., Condon, J. J., Schinnerer, E., et al. 2011, ApJ, 737, 67
Murray, A., van Kemenade, H., wiredfool, et al. 2023, python-pillow/Pillow, v10.0.1, Zenodo, doi:10.5281/zenodo.8349181
Nakajima, M., Negoro, H., Takagi, K., et al. 2025, GCN, 41410, 1
Nayana, A. J., & Chandra, P. 2014, GCN, 16815, 1
Newville, M., Otten, R., Nelson, A., et al. 2023, lmfit/lmfit-py, v1.2.2-đ, Zenodo, doi:10.5281/zenodo.8145703
Nicholl, M., Young, D. R., Aamer, A., et al. 2025, GCN, 41439, 1
Niemeyer, G., Pieviläinen, T., de Leeuw, Y., & Ganssle, P., 2021 dateutil/dateutil, v2.8.2 GitHub, https://github.com/dateutil/dateutil
Nugent, A. E., Fong, W.-f., Castrejon, C., et al. 2024, ApJ, 962, 5
Nugent, A. E., Villar, V. A., Gagliano, A., et al. 2025, arXiv:2509.08874
Oates, S. R., Marshall, F. E., Breeveld, A. A., et al. 2021, MNRAS, 507, 1296
O'Connor, B., Freeburn, J., Hall, X. J., et al. 2025, GCN, 41452, 1
Ohgami, T., Tominaga, N., Utsumi, Y., et al. 2021, PASJ, 73, 350
Oke, J. B., Cohen, J. G., Carr, M., et al. 1995, PASP, 107, 375
Paek, G. S. H., Im, M., Jeong, M., et al. 2025, ApJ, 981, 38
Pallets Projects., 2021 Flask–SQLAlchemy, v2.5.1, GitHub, https://github.com/pallets-eco/flask-sqlalchemy
Pallets Projects., 2022 Flask-SQLAlchemy, v2.5.1, GitHub, https://github.com/pallets/flask
Pang, P. T. H., Dietrich, T., Coughlin, M. W., et al. 2023, NatCo, 14, 8352
Pastorello, A., Kasliwal, M. M., Crockett, R. M., et al. 2008, MNRAS, 389, 955
Paterson, K., Lundquist, M. J., Rastinejad, J. C., et al. 2021, ApJ, 912, 128
Pearson, J., Hosseinzadeh, G., Sand, D. J., et al. 2023, ApJ, 945, 107
Pellegrino, C., Hiramatsu, D., Arcavi, I., et al. 2023, ApJ, 954, 35
Petrov, A., Larson, S. M., & Pradet, Q., 2023 urllib3/urllib3, v1.26.15, GitHub, https://github.com/urllib3/urllib3
Pian, E., D'Avanzo, P., Benetti, S., et al. 2017, Natur, 551, 67
Pillas, M., Antier, S., Ackley, K., et al. 2025, PhRvD, 112, 083002
Piro, A. L., Muhleisen, M., Arcavi, I., et al. 2017, ApJ, 846, 94
Plotly., 2023 plotly.py, v5.14.1, GitHub, https://github.com/plotly/plotly.py
Podsiadlowski, P., Hsu, J. J. L., Joss, P. C., & Ross, R. R. 1993, Natur, 364, 509
PostgreSQL Global Development Group., 2022 PostgreSQL, v14.6, https://www.postgresql.org/
Pozanenko, A. S., Minaev, P. Y., Grebenev, S. A., & Chelovekov, I. V. 2020, AstL, 45, 710
Prochaska, J. X., Hennawi, J. F., Westfall, K. B., et al. 2020a, JOSS, 5, 2308
Prochaska, J. X., Hennawi, J., Cooke, R., et al. 2020b, pypeit/PypeIt: Release 1.0.0, v1.0.0, Zenodo, doi:10.5281/zenodo.3743493
Python Packaging Authority, 2023 setuptools, v67.6.1, GitHub, https://github.com/pypa/setuptools
Qin, Y.-J., & Zabludoff, A. 2024, MNRAS, 533, 3517
Radice, D., Perego, A., Zappa, F., & Bernuzzi, S. 2018, ApJL, 852, L29
Rastinejad, J. C., Paterson, K., Fong, W., et al. 2022, ApJ, 927, 50
Rastinejad, J. C., Levan, A. J., Jonker, P. G., et al. 2025, ApJL, 988, L13
Reguitti, A., Pastorello, A., Smartt, S. J., et al. 2025, A&A, 698, A129
Reitz, K., 2023 Requests, v2.28.2, GitHub, https://github.com/psf/requests
Resmi, L., Schulze, S., Ishwara-Chandra, C. H., et al. 2018, ApJ, 867, 57
Rest, A., Stubbs, C., Becker, A. C., et al. 2005, ApJ, 634, 1103
Rhodes, L., Anderson, G. E., van der Horst, A. J., et al. 2023, GCN, 35097, 1
Rhodes, L., Smirnov, O., Mooley, K., & Woudt, P. 2025, GCN, 41666, 1
Ricci, R., Becerra, R. L., Troja, E. & ERC BHianca Team. 2025a, GCN, 41046, 1
Ricci, R., Yadav, M., & Troja, E. 2025b, GCN, 41464, 1
Ricci, R., Yadav, M., & Troja, E. 2025c, GCN, 41455, 1
Ricci, R., Yadav, M., Troja, E. & ERC BHianca Team. 2025d, GCN, 41542, 1
Richardson, L., 2023 Beautiful Soup, v4.12.2, Launchpad, https://launchpad.net/beautifulsoup/

Richmond, M. W., Treffers, R. R., Filippenko, A. V., et al. 1994, AJ, 107, 1022
Rudolf, N., Günther, H. M., Schneider, P. C., & Schmitt, J. H. M. M. 2016, A&A, 585, A113
Salgundi, A. 2025, Transient Name Server Discovery Report, 2025-3323, 1,
Santos, A., Bom, C. R., Kilpatrick, C. D., et al. 2025, GCN, 41501, 1
Santos, A., Kilpatrick, C. D., Bom, C. R., et al. 2024, MNRAS, 529, 59
Sapir, N., & Waxman, E. 2017, ApJ, 838, 130
Sarin, N., Hübner, M., Omand, C. M. B., et al. 2024, MNRAS, 531, 1203
Savchenko, V., Ferrigno, C., Kuulkers, E., et al. 2017, ApJL, 848, L15
Schechter, P. L., Mateo, M., & Saha, A. 1993, PASP, 105, 1342
Schlafly, E. F., & Finkbeiner, D. P. 2011, ApJ, 737, 103
Schlegel, D. J., Finkbeiner, D. P., & Davis, M. 1998, ApJ, 500, 525
Schroeder, G., Fong, W.-f., Kilpatrick, C. D., et al. 2025a, ApJ, 982, 42
Schroeder, G., Rastinejad, J., Fong, W., & Laskar, T. 2025b, GCN, 41038, 1
Schroeder, G., Rhodes, L., Fong, W., Laskar, T., & Berger, E. 2025c, GCN, 41060, 1
Schroeder, G., Rhodes, L., Laskar, T., et al. 2024, ApJ, 970, 139
SCiMMA Project, 2023 Hopskotch, https://scimma.org/hopskotch
Shappee, B. J., Prieto, J. L., Grupe, D., et al. 2014, ApJ, 788, 48
Shingles, L., Smith, K. W., Young, D. R., et al. 2021, TNSAN, 7, 1
Shrestha, M., Pearson, J., Wyatt, S., et al. 2024, ApJ, 961, 247
Shupe, D. L., Laher, R. R., Storrie-Lombardi, L., et al. 2012, SPIE, 8451, E1M
Singer, L., 2022 gracedb–sdk, v0.1.7, https://git.ligo.org/emfollow/gracedb-sdk
Singer, L. P., Parazin, B., Coughlin, M. W., et al. 2022, AJ, 163, 209
Singer, L. P., & Price, L. R. 2016, PhRvD, 93, 024013
Singer, L. P., Chen, H.-Y., Holz, D. E., et al. 2016a, ApJL, 829, L15
Singer, L. P., Chen, H.-Y., Holz, D. E., et al. 2016b, ApJS, 226, 10
Smartt, S. J., Chen, T. W., Jerkstrand, A., et al. 2017, Natur, 551, 75
Smith, D., 2022 crispy–bootstrap4, v2022.1, GitHub, https://github.com/django-crispy-forms/crispy-bootstrap4
Smith, K. W., Smartt, S. J., Young, D. R., et al. 2020, PASP, 132, 085002
Soares-Santos, M., Holz, D. E., Annis, J., et al. 2017, ApJL, 848, L16
Soderberg, A. M., Berger, E., Kasliwal, M., et al. 2006, ApJ, 650, 261
Sravan, N., Marchant, P., Kalogera, V., Milisavljevic, D., & Margutti, R. 2020, ApJ, 903, 70
Staley, T. D., 2014 voevent-parse: Parse, manipulate, and generate VOEvent XML packets-đ Astrophysics Source Code, ascl:1411.003
Stein, R. 2025, Transient Name Server Discovery Report, 2025-3264, 1,
Stein, R., Ahumada, T., Kasliwal, M., et al. 2025, GCN, 41414, 1
Stienstra, M., Takhteyev, Y., & Limberg, W., 2023 Python–Markdown, v3.4.3-đ, GitHub, https://github.com/Python-Markdown/markdown
STSCI Development Team., 2012 DrizzlePac: HST image software-đ Astrophysics Source Code Library, record ascl:1212.011
Subrayan, B. M., Sand, D. J., Bostroem, K. A., et al. 2025, ApJL, 990, L68
Swain, V., Anupama, G. C., Sahu, D. K., et al. 2025, GCN, 41837, 1
Tanaka, M., & Hotokezaka, K. 2013, ApJ, 775, 113
Tanvir, N. R., Levan, A. J., González-Fernández, C., et al. 2017, ApJL, 848, L27
Tartaglia, L., Fraser, M., Sand, D. J., et al. 2017, ApJ, 836, L12
Tebeka, M., 2022 fastavro, v1.6.1, GitHub, https://github.com/fastavro/fastavro
Thakur, A. L., Dichiara, S., Troja, E., et al. 2020, MNRAS, 499, 3868
Tody, D. 1986, SPIE, 627, 733
Tody, D. 1993, ASPC, 52, 173
TOM Toolkit Project, Collom, D., Lindstrom, L., & Nation, J., 2023 tom_nonlocalizedevents, v0.7.7,GitHub, https://github.com/TOMToolkit/tom_nonlocalizedevents
TOM Toolkit Project, Lindstrom, W., 2023 tom-alertstreams, v0.6.2, GitHub, https://github.com/TOMToolkit/tom-alertstreams
Tonry, J., Denneau, L., Weiland, H., et al. 2025, Transient Name Server Discovery Report, 2025-3286, 1,
Tonry, J. L., Denneau, L., Heinze, A. N., et al. 2018, PASP, 130, 064505
Trier, M., & van Oostveen, B., 2023 Django Extensions, v3.2.3, GitHub, https://github.com/django-extensions/django-extensions
Troja, E., O'Connor, B., & Becerra, R. L. 2025, GCN, 41506, 1
Troja, E., van Eerten, H., Ryan, G., et al. 2019, MNRAS, 489, 1919
Tucker, D. L., Wiesner, M. P., Allam, S. S., et al. 2022, ApJ, 929, 115
Usman, S. A., Nitz, A. H., Harry, I. W., et al. 2016, CQGra, 33, 215004
Valenti, S., Sand, D. J., Yang, S., et al. 2017, ApJ, 848, L24
Verheul, D., 2021 django-bootstrap4, v3.0.1, GitHub, https://github.com/zostera/django-bootstrap4
Vieira, N., Ruan, J. J., Haggard, D., et al. 2020, ApJ, 895, 96
Villar, V. A., Guillochon, J., Berger, E., et al. 2017, ApJ, 851, L21
Virtanen, P., Gommers, R., Oliphant, T. E., et al. 2020, NatMe, 17, 261
Waddington, T., 2020 django-gravatar, v1.4.4, GitHub, https://github.com/twaddington/django-gravatar
Watson, A. M., Butler, N. R., Lee, W. H., et al. 2020, MNRAS, 492, 5916
White, D. J., Daw, E. J., & Dhillon, V. S. 2011, CQGra, 28, 085016
Woosley, S. E., Eastman, R. G., Weaver, T. A., & Pinto, P. A. 1994, ApJ, 429, 300
Yaron, O., & Gal-Yam, A. 2012, PASP, 124, 668
Yoon, S.-C., Dessart, L., & Clocchiatti, A. 2017, ApJ, 840, 10
Young, D. 2023, fundamentals v2.4.1, Zenodo, doi: 10.5281/zenodo.8037510
Zhou, R., Ferraro, S., White, M., et al. 2023, JCAP, 2023, 097
Zonca, A., Singer, L., Lenz, D., et al. 2019, JOSS, 4, 1298